AGU PUBLICATIONS

JGR

Journal of Geophysical Research: Atmospheres

RESEARCH ARTICLE
10.1002/2017JD026688

Key Points:
- Adding aqueous chemistry to a LES model reduces OH by up to 25% and increases isoprene, promoting their segregation in clouds
- Covariance of isoprene oxidation products with OH changes sign (from positive to negative) when aqueous-phase reactions are included
- In-cloud formation of organic acids increases their mixing ratios throughout the boundary layer

Supporting Information:
- Supporting Information S1

Correspondence to:
Y. Li,
yanglibj@umich.edu

Citation:
Li, Y., Barth, M. C., Patton, E. G., & Steiner, A. L. (2017). Impact of in-cloud aqueous processes on the chemistry and transport of biogenic volatile organic compounds. *Journal of Geophysical Research: Atmospheres, 122*, 11,131–11,153. https://doi.org/10.1002/2017JD026688

Received 19 FEB 2017
Accepted 18 AUG 2017
Accepted article online 8 OCT 2017
Published online 19 OCT 2017

Impact of In-Cloud Aqueous Processes on the Chemistry and Transport of Biogenic Volatile Organic Compounds

Yang Li[1], Mary C. Barth[2], Edward G. Patton[2], and Allison L. Steiner[1]

[1]Climate and Space Sciences and Engineering, University of Michigan, Ann Arbor, MI, USA, [2]National Center for Atmospheric Research, Boulder, CO, USA

Abstract We investigate the impacts of cloud aqueous processes on the chemistry and transport of biogenic volatile organic compounds (BVOC) using the National Center for Atmospheric Research's large-eddy simulation code with an updated chemical mechanism that includes both gas- and aqueous-phase reactions. We simulate transport and chemistry for a meteorological case with a diurnal pattern of nonprecipitating cumulus clouds from the Baltimore-Washington area DISCOVER-AQ campaign. We evaluate two scenarios with and without aqueous-phase chemical reactions. In the cloud layer (2–3 km), the addition of aqueous phase reactions decreases HCHO by 18% over the domain due to its solubility and the fast depletion from aqueous reactions, resulting in a corresponding decrease in radical oxidants (e.g., 18% decrease in OH). The decrease of OH increases the mixing ratios of isoprene and methacrolein (MACR) (100% and 15%, respectively) in the cloud layer because the reaction rate is lower. Aqueous-phase reactions can modify the segregation between OH and BVOC by changing the sign of the segregation intensity, causing up to 55% reduction in the isoprene-OH reaction rate and 40% reduction for the MACR-OH reaction when clouds are present. Analysis of the isoprene-OH covariance budget shows the chemistry term is the primary driver of the strong segregation in clouds, triggered by the decrease in OH. All organic acids except acetic acid are formed only through aqueous-phase reactions. For acids formed in the aqueous phase, turbulence mixes these compounds on short time scales, with the near-surface mixing ratios of these acids reaching 20% of the mixing ratios in the cloud layer within 1 h of cloud formation.

1. Introduction

Clouds affect the chemical composition of the troposphere by various chemical and physical processes (e.g., Ervens, 2015; Tost et al., 2010). Aqueous-phase reactions in clouds provide an additional pathway for altering the composition in and near clouds, creating unique intermediates such as ions and hydrated species that are distinct from the products created from gas-phase only chemistry (Ervens, 2015). Convective motions in clouds vertically transport temperature and water vapor (Cotton et al., 1995), and chemical constituents (e.g., Barth et al., 2007; Vilà-Guerau de Arellano et al., 2005) from the turbulent subcloud layer directly influenced by the surface to the nonturbulent free-troposphere above.

Investigations into acid rain production highlighted the importance of in-cloud aqueous-phase chemistry. Many observational studies showed the importance of sulfate formation from the aqueous-phase oxidation of sulfur dioxide (SO_2) (e.g., Bower et al., 1999; Hegg & Hobbs, 1979, 1981, 1982; Husain, 1989; Husain et al., 2004; Laj et al., 1997). Based on box modeling studies, Chameides (1984) and Jacob (1986) found that the in-cloud acidity affected not only the generation of inorganic acids (e.g., sulfuric acid) but also the formation of organic acids. Early regional chemistry transport models were developed to study the regional-scale transport, chemistry, and deposition of the chemical constituents contributing to acid rain based on parameterized chemical reactions and cloud processes (Carmichael & Peters, 1986; Chang et al., 1987). Lelieveld and Crutzen (1990, 1991) found that in-cloud aqueous-phase chemistry could influence the photochemistry of the troposphere by reducing HCHO, HO_x, and O_3 substantially (15–70% for HCHO, 10–70% for HO_x, and 35–45% for O_3). However, Liang and Jacob (1997) used a lower but more realistic cloud liquid water and a lower Henry's law constant for CH_3O_2 and simulated less than 3% reduction in O_3 due to cloud chemistry. Similarly, Barth et al. (2002) showed a 6% O_3 reduction caused by aqueous chemistry and cloud radiative effects. Up until this point, only CH_4 and HCHO chemistry were included to investigate the in-cloud aqueous chemistry of organic trace species.

The role of chemical processing of organic compounds in clouds is gaining increasing importance because of the implications of these organic compounds to form secondary organic aerosol (SOA). Sempére and Kawamura (1994) studied aerosol samples in the atmosphere with observations, suggesting the importance of organics (e.g., oxalic acid, glyoxal, and methylglyoxal) for the formation of SOA in aqueous chemistry. Jacob and Wofsy (1988) found isoprene gas and aqueous chemistry provided an important atmospheric source of formic acid, methacrylic acid, and pyruvic acid over the Amazon forest. Further laboratory studies (Carlton et al., 2007; Ervens et al., 2003) solidified that the aqueous-phase photooxidation of organics (e.g., glyoxal) is a potential global and regional source of SOA, and regional scale modeling showed that inclusion of cloud processing of organics (e.g., glyoxal and methylglyoxal) improved correlations between modeled and aircraft-observed organic aerosols (Carlton et al., 2008). Other studies (Chen et al., 2007; Ervens et al, 2011; Lim et al., 2010) investigated the importance of aqueous-phase formed SOA-precursor organic acids (e.g., hydroxyacetic acid, glyoxylic acid, oxalic acid, and pyruvic acid) but were limited in that the vertical mixing in their simulations was parameterized and assumed that each grid cell was well mixed.

In this study, we focus on the gas and aqueous chemistry of BVOC as the they are ubiquitous (Guenther et al., 1995) and reactive in the atmosphere (Goldstein & Galbally, 2007). BVOC play a crucial role in the formation of O_3 through a series of photochemical reactions in the presence of NO_x ($NO + NO_2$) and also control the oxidizing capacity of the atmosphere through OH and HO_2 radical chemistry (Atkinson, 2000; Lelieveld et al., 2008). Gas-phase oxidation of primary emitted BVOC may result in functionalized products with lower volatility that have the ability to partition to the aqueous phase. For example, the BVOC primary oxidation products, methyl vinyl ketone (MVK), and methacrolein (MACR) can react in the aqueous phase to produce low-volatility products (e.g., small carbonyl compounds including oxalate, glyoxal, and methylglyoxal), providing an important source of secondary organic aerosol (SOA) (Blando & Turpin, 2000; Ervens et al., 2011; Fu et al., 2008). The efficacy of this process at the cloud scale and its importance in regional and global models are still poorly understood. Because these reactions are occurring in clouds, accurate model representation of clouds, turbulence, and multiphase chemistry is required to understand the fates and distributions of the BVOC species and its relevance for SOA formation.

Representing the physical processes within clouds requires a wide range of spatial (micrometers to kilometers) and temporal scales (Hozumi et al., 1982; Leriche et al., 2013; Plank, 1969). Efficient upward transport in convective clouds occurs on timescales of minutes to hours, much faster than the timescale of days to reach the upper troposphere by advection or diffusion (Barth et al., 2001; Tost et al., 2010). A range of spatial scales have been used to investigate cloud-chemistry interactions, ranging from zero-dimensional box modeling of coupled gas- and aqueous-phase chemistry (e.g., Barth et al., 2003; Chameides, 1984) up to three-dimensional regional models with parameterized cloud processes to study acid rain and aerosol formation (Chang et al., 1987; Chapman et al., 2009). Prior regional and global three-dimensional modeling studies have incorporated aqueous mechanisms including the cloud aqueous processing of organic chemical constituents (e.g., isoprene oxidation products) at varying spatial and time scales. At coarser spatial resolutions in global models (e.g., the GEOS-Chem model with a 2° latitude × 2.5° longitude resolution, Fu et al., 2009; Marais et al., 2016) and regional models (e.g., the regional scale Community Multiscale Air Quality (CMAQ) model with a horizontal resolution of 36 km, Chen et al., 2007), clouds are parameterized by predicting the cloud fraction within each grid. At finer regional resolutions ($<$4 km), many simulations assume that clouds are resolved and utilize grid sizes of the same order as large clouds (km) and solve the meteorology and chemistry on the order of minutes. For example, previous studies implemented the Weather Research and Forecasting model coupled with Chemistry (WRF-Chem) at cloud-resolving scales (~2 km) but found a low bias in reproducing SOA precursors caused by a lack of detailed cloud aqueous chemistry scheme (Chapman et al., 2009; Tuccella et al., 2015). Berg et al. (2015) and Wang et al. (2015) improved the WRF-Chem treatment of cloud aqueous chemistry for subgrid parameterized convective clouds for coarser resolutions (10 km and 36 km horizontal grid resolutions, respectively) to compensate for the computational expense. In all of these studies, the model resolution and its treatment of clouds are key factors in evaluating the impacts of cloud processes on VOC chemistry and transport. However, these studies are limited by the lack of a combination between an accurate representation of the turbulent motion of clouds in conjunction with sophisticated multiphase chemistry.

Because most atmospheric reactions are driven by kinetics, the proximity of molecules is required for chemical reactions to occur. Further, because dispersion within the atmospheric boundary layer (ABL) is controlled primarily by ABL-scale eddies, incomplete mixing becomes important for reactions when the reaction rate is similar to the turbulent mixing rate (Schumann, 1989; Sykes et al., 1994). As a result, segregation, defined as the reduction in chemical reaction rates caused by incomplete mixing (e.g., Krol et al., 2000), can occur for fast reactions within the ABL. In clouds, the partitioning of soluble species into the aqueous phase affects the interstitial gas phase mixing ratios and potential reaction rates. Segregation can also happen between soluble species and less soluble species. For example, because HO_2 is taken up by cloud water and NO is insoluble, the reaction rate between NO and HO_2 may decrease due to segregation, reducing the recycling rate of HO_2 to OH and the production of gas-phase OH, thereby further suppressing ozone (O_3) formation and altering other oxidants in the atmosphere (Lelieveld & Crutzen, 1990). Many studies have investigated the intensity of segregation in dry boundary layers using observations and models with gas chemistry only and found a turbulence-induced reduction in their reaction rates in the subcloud layer (e.g., Kim et al., 2016; Krol et al., 2000; Molemaker & Vilà-Guerau de Arellano, 1998; Ouwersloot et al., 2011). Vilà-Guerau de Arellano et al. (2005) discussed the segregation induced by clouds using a LES without aqueous chemistry and attributed all segregation to cloud transport. Kim et al. (2004) also found enhanced segregation in shallow cumulus clouds and proposed that in-cloud aqueous processes could play an important role in segregation, although aqueous reactions were not included in their simulations. Therefore, a model with high resolution and detailed gas and aqueous chemical mechanisms are required to study the effects of clouds on chemistry in convective environments.

In this study, we utilize the National Center for Atmospheric Research's (NCAR) large-eddy simulation (LES) model coupled to the NCAR gas-phase chemical mechanism MOZART2.2 (Kim et al., 2012) (which will hereafter be called LES-Chem). We add an updated aqueous-phase chemical mechanism (Barth et al., 2003; Barth et al., 2016; Herrmann et al., 2010; Herrmann et al., 2015) to simulate and understand the effects of aqueous-phase chemistry on vertical distributions of key BVOC species, such as isoprene and its gas-phase oxidation products, in convective environments. LES-Chem has vertical and horizontal resolutions that can resolve the energy-containing turbulent eddies in the ABL (Moeng, 1984), and the coupled online chemical mechanism provides a detailed description of gas and aqueous phase organic chemistry. In this manuscript, we present high-resolution LES-Chem simulations representing both convective transport and aqueous phase chemistry and their impact on the oxidation and distribution of organic species. As far as we are aware, this study represents the first to include aqueous chemistry in a LES to study the interplay between ABL dynamics and chemistry.

2. Methods

2.1. Simulation Design

We use the NCAR LES (Moeng, 1984, 1987; Patton et al., 2005) with an online chemical mechanism (Kim et al., 2012; Kim et al., 2016; Li et al., 2016) to study the impacts of clouds on gas and aqueous chemistry. Li et al. (2016) simulated cloud and chemical composition evolution with this model for the NASA DISCOVER-AQ Baltimore-Washington campaign for three different meteorological case studies, including one clear case and two convective cases. Case 1 has fair weather without cloud formation, therefore making it inappropriate for this study of aqueous processes. Case 3 has strong convection with cumulus cloud formation. Choosing Case 3 would likely produce similar results compared to Case 2 with regard to the effects of aqueous processes. However, a taller domain would be needed for Case 3 in order to permit the simulated clouds to remain largely independent of the top boundary. Increasing the domain height while maintaining similar computational cost would require lowering our resolution or limiting the chemical processes, which would reduce our confidence in the results and would thus prefer to avoid. We select Case 2 from those experiments (11 July 2011, 0530–1430 LT), as it has a clear diurnal pattern of nonprecipitating cumulus clouds with the cloud fraction peaking around 40% at midday (Li et al., 2016). This specific case provides a unique opportunity to examine the BVOC distribution and chemistry under convective conditions.

In this simulation, Li et al. (2016) used meteorological initial and boundary conditions from the global Modern-Era Retrospective analysis for Research and Applications (MERRA) reanalysis (Rienecker et al., 2011), and chemical initial and boundary conditions from averaged NASA P-3B measurements above the

Fair Hill, Maryland, site on the case study day. While the Li et al. (2016) study used a model domain of 14.4 km × 14.4 km × 6.4 km (96 × 96 × 96 grid points with horizontal grid spacing of 150 m and vertical grid spacing of 66.67 m), here we use a lower domain height (4.8 km) and test three horizontal resolutions (see section 2.2). The 4.8 km domain height allows full turbulence development independent of the top boundary (Li et al., 2016) and captures the varying cloud layers ranging from 1 km to 4 km altitudes. The interaction between clouds and radiation is not explicitly included in these simulations. Incident radiation at the surface is assumed to be horizontally homogeneous but time varying by imposing the bulk variation of the sensible and latent heat fluxes, and as a result, there is no local cloud impact on the available energy determining surface exchange. In addition, radiation incident on the surface does not influence reactant emissions in these simulations. However, the simulation is influenced by an imposed radiative tendency based on MERRA reanalysis (Li et al., 2016) which introduces a horizontally homogeneous radiatively induced heating/cooling to each vertical level which does influence turbulent motions. There is no direct impact on turbulence from the cloud-induced modulation of radiation. The simulation is performed with a fixed time step of 1.5 s, and meteorological simulations begin at 0530 LT with chemistry initiated at 0830 LT. Li et al. (2016) provide further details of the LES meteorological configuration.

The gas-phase chemistry mechanism is based on the NCAR gas-phase chemical mechanism MOZART2.2 (Horowitz et al., 2003) as implemented by Kim et al. (2012). It includes 64 reactants and 168 reactions. Although the isoprene chemistry does not include the most recent research (e.g., Paulot et al., 2009; Paulot et al., 2012), a comparison of the mechanism used here with an updated isoprene mechanism using a photochemical box model finds consistent behavior between the two mechanisms for the relationship between NO_x and OH (Kim et al., 2016). The aqueous-phase chemical mechanism (Table 1) is based on Barth et al. (2003) and Barth et al. (2016). For the current LES-Chem study, we updated reactions and rate constants based on Ervens et al. (2008), Herrmann et al. (2010), and Herrmann et al. (2015) and added organic acid formation in the aqueous phase based on Ervens et al. (2008). Henry's law equilibrium constants (Table 2) are based on Sander (2015) and Sander et al. (2011). Accommodation coefficients (Table 2) are based on McNeill et al. (2012). Details on the calculations of chemical production and loss for the LES chemical mechanism are provided in the supporting information. The method used to partition trace gas mixing ratios between the gas and aqueous phases works well for both low and high-solubility gases, but it overestimates OH aqueous-phase concentrations, which are controlled by the chemistry and mass transfer rather than the Henry's Law equilibrium. Therefore, the conclusions drawn here from the OH chemical budget are qualitative rather than quantitative. Isoprene emissions are calculated based on the solar zenith angle and temperature (Guenther et al., 2006), and anthropogenic VOC emissions are not included in these simulations.

We categorize the BVOC species following Li et al. (2016) as (1) primary emitted BVOC (isoprene), (2) primary oxidation products (MVK, MACR, and isoprene hydroxyhydroperoxide (ISOPOOH)), (3) dual-oxidation products (produced by both the primary emitted BVOC and the oxidation products, such as formaldehyde (HCHO)), and (4) secondary oxidation products (produced by the primary oxidation products, including hydroxyacetone (HYAC), glycolaldehyde (GLYALD), methylglyoxal (MGLY), and acetaldehyde (ACETALD)). To understand aqueous processes, we also categorize the VOC species according to the Henry's law constants as (1) insoluble species (isoprene), (2) slightly soluble species (MACR, ACETALD, MVK, and ISOPOOH with a $K_H^{\ominus}$ (defined as Henry's law constant K_H at 298 K) range of 4.8–300 M atm^{-1}), (3) moderately soluble species (HYAC, HCHO, MGLY, GLYALD, and ACETAC (CH_3COOH) with a $K_H^{\ominus}$ range of 3,230–7,700 M atm^{-1}), and (4) highly soluble organic acids (hydroxyacetic acid (GLYCAC), formic acid (HCOOH), glyoxylic acid (GLYOXAC), pyruvic acid (PYRAC), and oxalic acid (OXALAC) with a $K_H^{\ominus}$ range of 8,900–5.0 × 10^8 M atm^{-1}).

To understand the importance of including aqueous-phase reactions in the LES chemical scheme, we simulate two scenarios using the meteorological and chemical environment described above, including (1) with gas phase chemistry only and aqueous-phase reactions turned off (scenario 1: NOAQU) and (2) with both gas- and aqueous-phase reactions (scenario 2: AQU).

2.2. Comparison of Three LES Resolutions

For a typical daytime convective PBL, Sullivan and Patton (2011) investigated the sensitivity and convergence of the LES and found simulations for a model domain of 5120 m × 5120 m × 2048 m with 256^3 mesh points (with a $\Delta x \times \Delta y \times \Delta z$ of 20 m × 20 m×8 m) or more were needed to estimate the high-order moments of

Table 1
Aqueous-Phase Reactions

Number	Reaction	k_{298}	E/R
A1	$O_3 + h\nu + H_2O \rightarrow H_2O_2 + O_2$		
A2	$H_2O_2 + h\nu \rightarrow 2\ OH$		
A3	$HCHO + OH + O_2 \rightarrow HCOOH + HO_2$	1.0×10^9	1,000
A4[a]	$HCOOH + OH + O_2 \rightarrow CO_2 + HO_2 + H_2O$	1.3×10^8	1,000
	$HCOO^- + OH + O_2 \rightarrow CO_2 + HO_2 + OH^-$	3.2×10^9	1,000
A5	$CH_3O_2 + O_2^- + H_2O \rightarrow CH_3OOH + OH^- + O_2$	5.0×10^7	1,600
A6	$CH_3OOH + OH \rightarrow CH_3O_2 + H_2O$	2.4×10^7	1,700
A7	$CH_3OOH + OH \rightarrow CH_3(Oh)_2 + HO_2$	6.0×10^6	1,700
A8[a]	$HO_2 + HO_2 \rightarrow H_2O_2 + O_2$	8.3×10^5	2,720
	$O_2^- + HO_2 + H_2O \rightarrow H_2O_2 + OH^- + O_2$	9.7×10^7	1,060
A9	$OH + OH \rightarrow H_2O_2$	5.2×10^9	1,500
A10	$O_3 + HO_2 \rightarrow OH + 2O_2$	1.5×10^9	2,200
A11	$O_3 + OH \rightarrow HO_2 + O_2$	3.0×10^9	1,500
A12	$H_2O_2 + OH \rightarrow HO_2 + H_2O$	3.0×10^7	1,700
A13	$OH + HO_2 \rightarrow H_2O + O_2$	1.0×10^{10}	1,500
A14	$CO_2 + 2OH^- \rightarrow CO_3^{2-} + H_2O$	1.0×10^7	1,500
A15	$CO_2 + HO_2 + 2OH^- \rightarrow H_2O_2 + CO_3^{2-} + OH$	1.5×10^6	1,500
A16	$CO_3^{2-} + H_2O_2 + OH \rightarrow HO_2 + CO_2 + 2OH^-$	8.0×10^5	2,800
A17	$CO_3^{2-} + HO_2 \rightarrow CO_2 + OH^- + O_2^-$	4.0×10^8	1,500
A18	$NO_3 + HO_2 \rightarrow HNO_3 + O_2$	1.0×10^9	1,500
A19	$N_2O_5 + H_2O \rightarrow 2\ HNO_3$	1.0×10^{20}	0
A20	$SO_2 + H_2O_2 \rightarrow SO_4^{2-} + 2H^+$	7.2×10^7	4,000
A21[a]	$SO_2 + 2O_3 \rightarrow SO_4^{2-} + 2O_2$	2.4×10^4	0
	$HSO_3^- + O_3 + OH^- \rightarrow SO_4^{2-} + H_2O + O_2$	3.7×10^5	5,530
	$SO_3^{2-} + O_3 \rightarrow SO_4^{2-} + O_2$	1.5×10^9	5,280
A22	$OH + CHOCHO \rightarrow HO_2 + GLYOXAC$	9.2×10^8	1,200
A23[a]	$OH + GLYOXAC \rightarrow HO_2 + OXALAC$	3.6×10^8	1,000
	$OH + GLYOX^- \rightarrow HO_2 + OXALAC + Oh^-$	2.9×10^9	4,300
A24	$OH + MGLY \rightarrow HO_2 + 0.92\ PYRAC + 0.08\ GLYOXAC$	6.1×10^8	1,400
A25	$OH + GLYALD \rightarrow HO_2 + GLYCAC$	1.2×10^9	0
A26	$OH + GLYCAC \rightarrow HO_2 + GLYOXAC$	1.2×10^9	0
A27[a]	$OH + OXALAC \rightarrow HO_2 + 2\ CO_2 + H_2O$	1.4×10^6	0
	$OH + OXAL^- \rightarrow HO_2 + 2\ CO_2 + OH^-$	1.9×10^8	2,800
	$OH + OXAL^{2-} \rightarrow O_2^- + 2\ CO_2 + OH^-$	1.6×10^8	4,300
A28[a]	$OH + PYRAC \rightarrow HO_2 + ACETAC + H_2O$	3.2×10^8	1,800
	$OH + PYR^- \rightarrow HO_2 + ACET^- + CO_2$	7.1×10^8	3,000
A29[a]	$OH + ACETAC \rightarrow HO_2 + 0.15\ HCHO + 0.85\ GLYALD + H_2O$	1.5×10^7	1,330
	$OH + ACET^- \rightarrow HO_2 + 0.15\ HCHO + 0.85\ GLYALD + OH^-$	1.0×10^8	1,800
A30	$CH_3O_2 + CH_3O_2 \rightarrow HCHO + CH_3OH + O_2$	1.7×10^8	2,200
A31	$OH + ACETALD + O_2 \rightarrow HO_2 + ACETAC$	3.6×10^9	580
A32	$OH + HYAC + O_2 \rightarrow HO_2 + MGLY + H_2O$	1.3×10^8	0
A33	$2OH + CHOCHO \rightarrow 2\ HCOOH$	5.0×10^3	0
A34	$H_2O_2 + CHOCHO \rightarrow 2\ HCOOH$	1.0	0
A35[a]	$H_2O_2 + GLYOXAC \rightarrow HCOOH + CO_2 + H_2O$	9.0×10^{-1}	0
	$H_2O_2 + GLYOX^- \rightarrow HCOO^- + CO_2 + H_2O$	1.6×10^1	0
A36	$H_2O_2 + HCOOH \rightarrow CO_2 + 2H_2O$	2.0×10^{-1}	0
A37[a]	$H_2O_2 + OXALAC \rightarrow 2\ CO_2 + 2H_2O$	1.1×10^{-1}	0
	$H_2O_2 + OXAL^- \rightarrow 2\ CO_2 + OH^- + H_2O$	1.5×10^{-4}	0
A38[a]	$H_2O_2 + PYRAC \rightarrow ACETAC + CO_2 + H_2O$	1.1×10^{-1}	0
	$H_2O_2 + PYR^- \rightarrow ACET^- + CO_2 + H_2O$	7.5×10^{-1}	0
A39	$OH + CH_3OH \rightarrow CH_2OH + H_2O$	9.0×10^8	0
A40	$OH + CH_3COCH_3 + O_2 \rightarrow CH_3COCH_2O_2 + H_2O$	1.3×10^8	0

conserved scalars from the resolved LES flow fields and resolve sharp gradients in scalars such as temperature. Based on these resolution tests, a higher LES resolution than that implemented by Li et al. (2016) may be necessary to accurately resolve the turbulent environment. Based on the fixed domain (14.4 km × 14.4 km × 4.8 km) described above, we test three mesh resolutions to examine the numerical convergence of the idealized LES simulations in the absence of chemistry.

Table 1.
(Continued)

Number	Reaction	k_{298}	E/R
A41	OH + isoprene + O_2 → $ISOPO_2$ + H_2O	1.4×10^{10}	0
A42	OH + MACR + O_2 → $CH_3COCHO_2CH_2OH$ + H_2O	9.4×10^{9}	1,200
A43	OH + MVK + O_2 → $CH_3COCHO_2CH_2OH$ + H_2O	7.3×10^{9}	1,400
A44	O_3 + MACR → MGLY + HCHO + 0.70 H_2O_2	2.4×10^{4}	2,900
A45	O_3 + MVK → 0.75 MGLY + HCHO + 0.24 PYRAC + 0.69 H_2O_2	4.4×10^{4}	2,200

Note. Reaction rates are calculated using equation $k = k_{298} \times e^{\left[\frac{E}{R}\left(\frac{1}{298}-\frac{1}{T}\right)\right]}$. The units are s^{-1} for the photolysis rates and $M^{-1}\ s^{-1}$ for the second-order reactions. The mechanism names are explained as follows: Isoprene: C_5H_8, $ISOPO_2$: peroxy radical derived from OH + isoprene or $HOCH_2COOCH_3CHCH_2$, ISOPOOH: hydroxyhydroperoxide or $HOCH_2COOHCH_3CHCH_2$, MACR: methacrolein or CH_2CCH_3CHO, MVK: methyl vinyl ketone or $CH_2CHCOCH_3$, HYAC: hydroxyacetone or CH_3COCH_2OH, GLYALD: glycolaldehyde or $HOCH_2CHO$, MGLY: methylglyoxal or CH_3COCHO, ACETALD: acetaldehyde or CH_3CHO, GLYCAC: hydroxyacetic acid or $HOCH_2COOH$, GLYOXAC: glyoxylic acid or CHOCOOH, PYRAC: pyruvic acid or $CH_3COCOOH$, OXALAC: oxalic acid or HOOCCOOH, ACETAC: acetic acid or CH_3COOH.
[a]The reaction family is solved for using the dissociation constants (Ervens et al., 2008) to partition between ions.

Three resolutions were tested with a constant spacing for each mesh: (1) 96^3 grid points, representing a $\Delta x \times \Delta y \times \Delta z$ of 150 m × 150 m×50 m, (2) 192^3 grid points, representing a $\Delta x \times \Delta y \times \Delta z$ of 75 m ×75 m ×25 m, and (3) 320^3 grid points, representing 45 m ×45 m×15 m, to capture a range of resolutions within our computational resources. In these three varying-resolution simulations, clouds in the 192^3 and 320^3 simulations exhibit similar evolution patterns (Figure 1). As in Li et al. (2016), the cloud top is defined as the maximum height where liquid water is present in the domain and the cloud base is defined as the minimum height where liquid water is present (Figure 1a). The cloud fraction is the horizontal fraction of the domain containing vertically integrated liquid water (or LWP > 0; Figure 1b). Clouds in the 192^3 and 320^3 simulations develop around 1045 LT (Figure 1a) and reach the highest fraction (47%) at around 1130 LT (Figure 1b). Clouds in the 96^3 simulation form slightly earlier (Figure 1a), and the cloud fraction in the 96^3 simulation diverges from the other two simulations with higher resolutions (Figure 1b). Cloud fraction diverges ($<$10%) between the 192^3 and 320^3 simulations after 1200 LT (Figure 1b), with the 320^3 simulation simulating a slightly higher cloud fraction. The divergence of the cloud fraction between the 192^3 and 320^3 resolutions after 12 LT results from the fact that the coarser resolution simulations do not resolve scalar gradients as well as the higher resolution simulations; therefore, there are fewer updrafts in the coarse simulation compared to the finer grids. Since the initial conditions are such that the free troposphere is drier than the subcloud boundary layer, the finer resolution simulations entrain more moist air aloft, condensing into cloud. Therefore, fewer clouds form and persist for shorter duration in the coarser-resolution simulations compared to those in the finer-resolution simulations.

As in the statistical analysis of Sullivan and Patton (2011), we select three time periods to compare the behaviors of the three resolutions after the turbulence is spun-up, representing (1) clear weather conditions before cloud formation (1000 LT), (2) a convective condition with peak cloud fraction (1200 LT), and (3) a weaker convective environment with dissipating clouds (1300 LT). For each vertical level, the mean values represent horizontally averaged quantities (over the entire horizontal domain) that are temporally averaged for 30 min time periods surrounding the desired time (i.e., 0945–1015 LT, 1145–1215 LT, and 1245–1315 LT). To investigate turbulent quantities, we define a fluctuation as a quantity's deviation from its instantaneous horizontal average.

To investigate the resolution dependence of the LES in simulating turbulence, we examine the total (resolved plus subgrid scale, SGS) quantities of important meteorological statistics, including liquid water potential temperature flux (WH), total water (vapor plus liquid) specific humidity flux (WQ), and turbulent kinetic energy (TKE). Liquid water potential temperature is a thermodynamic variable that is conserved in the absence of precipitation (Betts, 1973; Deardorff, 1976a), and reverts to potential temperature in the absence of liquid water. This thermodynamic variable is frequently used in nonprecipitating cloud simulation models. We note that liquid water potential temperature and total water specific humidity are conserved when undergoing reversible processes (Deardorff, 1976b). SGS contributions to WH, WQ, and TKE are estimated using a SGS eddy viscosity model (Deardorff, 1980).

The variation of WH, WQ, and TKE from 1000 LT to 1200 LT to 1300 LT (Figure 2) is consistent with the cloud evolution in Figure 1. Cloud development at the two later times produces larger fluxes and TKE at high

Table 2
Henry's Law Constants and Accommodation Coefficients for Trace Gases That Dissolve in Water as a Solvent

Chemical species	Accommodation coefficient	$K_H^{\ominus}$ (M atm^{-1})	$-d \ln K_H/d(1/T)$, K
O_3	0.00053	1.03×10^{-2}	2830
NO_2	0.00063	1.2×10^{-2}	2360
NO	0.005	1.91×10^{-3}	1790
HNO_3	0.2	2.6×10^{6}	8700
H_2O_2	0.02	8.44×10^{4}	7600
CH_3OOH	0.0038	3.0×10^{2}	5280
HCHO	0.2	3.23×10^{3}	7100
SO_2	0.11	1.23	3120
OH	0.05	3.9×10^{1}	0
CH_3CO_3	0.02	1.0×10^{-1}	0
HNO_4	0.2	1.2×10^{4}	6900
HO_2	0.2	6.9×10^{2}	0
N_2O_5	0.005	1.0×10^{12}	0
NO_3	0.001	3.8×10^{-2}	0
CH_3O_2	0.05	2.7	2030
$CH_3CO_3NO_2$	0.02	2.8	5730
$CH_2CCH_3CO_3NO_2$	0.02	1.7	0
MACR[a]	0.02	4.8	4300
MVK[a]	0.02	2.6×10^{1}	4800
ACETALD[a]	0.03	1.29×10^{1}	5890
C_3H_6OHOOH	0.05	3.36×10^{2}	5995
CH_3COOOH	0.02	8.37×10^{2}	5310
CHOCHO	0.023	4.19×10^{5}	7480
C_2H_5OOH	0.05	3.36×10^{2}	5995
GLYALD[a]	0.023	4.1×10^{4}	4600
MGLY[a]	0.023	3.4×10^{3}	7500
$CH_2CCH_3CHONO_2CH_2OH$	0.02	1.0×10^{3}	0
$HOCH_2CCH_3CHCHO$	0.03	3.0×10^{4}	9200
CH_3OH	0.015	2.03×10^{2}	9240
CH_3COCH_3	0.02	2.78×10^{1}	5530
$C_{10}H_{18}O_3$	0.05	3.0×10^{2}	5280
$CH_3COCHOOHCH_2OH$	0.05	3.0×10^{2}	5280
HYAC[a]	0.02	7.7×10^{3}	0
CH_3COCH_2OOH	0.05	3.0×10^{2}	5280
$HOCH_2COOHCH_3CHCHOH$	0.05	3.0×10^{2}	5280
ISOPOOH[a]	0.05	3.0×10^{2}	5280
HCOOH	0.012	8.9×10^{3}	6100
SO_4^{2-}	0.2	1.0×10^{12}	0
CO_2	0.05	3.6×10^{-2}	2200
CO_3^{2-}	0.1	1.0×10^{12}	0
CH_3COOH	0.019	5.5×10^{3}	0
GLYCAC[a]	0.019	2.83×10^{4}	0
GLYOXAC[a]	0.019	1.0×10^{4}	0
PYRAC[a]	0.019	3.1×10^{5}	5088
OXALAC[a]	0.019	5.0×10^{8}	0

[a]The mechanism names are explained as follows: MACR: methacrolein or CH_2CCH_3CHO, MVK: methyl vinyl ketone or $CH_2CHCOCH_3$, HYAC: hydroxyacetone or CH_3COCH_2OH, GLYALD: glycolaldehyde or $HOCH_2CHO$, MGLY: methylglyoxal or CH_3COCHO, ACETALD: acetaldehyde or CH_3CHO, GLYCAC: hydroxyacetic acid or $HOCH_2COOH$, GLYOXAC: glyoxylic acid or CHOCOOH, PYRAC: pyruvic acid or $CH_3COCOOH$, OXALAC: oxalic acid or HOOCCOOH, ISOPOOH: hydroxyhydroperoxide or $HOCH_2COOHCH_3CHCH_2$.

altitudes (1–3 km, Figures 2d–2i). At 1200 LT and 1300 LT, WH, WQ, and TKE show more divergence between simulations with different resolutions. In general, WH and TKE profiles show better convergence between the two finer-mesh simulations (192^3 and 320^3; Figures 2d, 2f, 2g, and 2i). At 1300 LT, we find in the cloud layer that WQ diminishes with increasing resolution (Figure 2h). Those discrepancies within 1–3 km highlight the resolution sensitivity of the LES, indicating that coarser model resolutions may overestimate moisture transport by clouds and thus potentially overestimate aqueous chemical reaction rates within cloud layers.

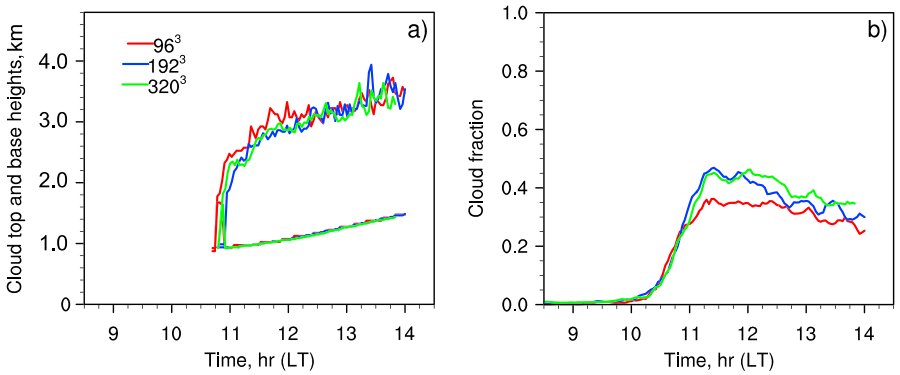

Figure 1. Temporal evolution of (a) domain maximum cloud top and base heights and (b) the cloud fraction (unitless) over the model domain for the three simulations with grid points of 96^3, 192^3, and 320^3.

In summary, the statistics effectively converge with the 192^3 mesh resolution or higher, although there are some minor differences between the 192^3 and 320^3 mesh resolutions. We also note that these tests do not necessarily reflect resolution independence for the chemical reactants; however, there is little difference between the 96^3 and 192^3 grids for the vertical profiles of reactive species such as isoprene and chemical segregation values (<2%, results not shown). The high computational expense associated with including both gas- and aqueous-phase reactions makes the 320^3 grid mesh simulations impractical to perform within our available resources. We therefore select the 192^3 mesh for our simulations investigating the importance of aqueous-phase chemistry within clouds.

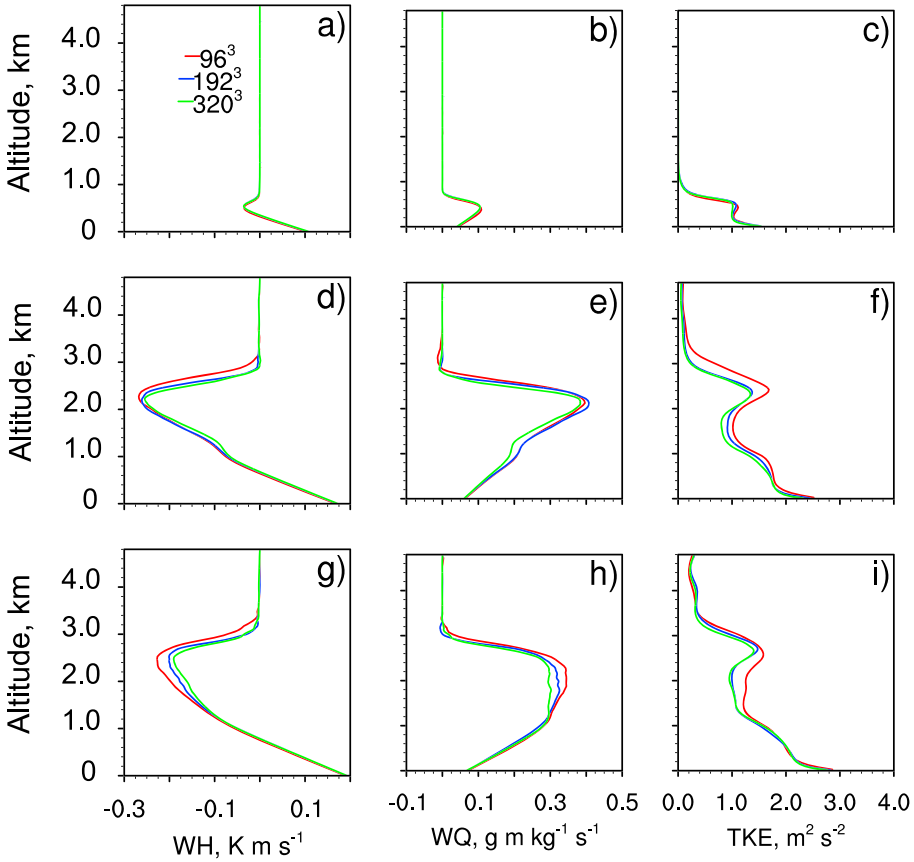

Figure 2. Vertical profiles of total (resolved plus SGS) quantities of (a, d, and g) liquid water potential temperature flux (WH), (b, e, and h) total water (vapor plus liquid) specific humidity flux (WQ), and (c, f, and i) turbulent kinetic energy (TKE) horizontally averaged over the model domain and averaged over a 30 min period at 1000 LT (Figures 2a–2c), 1200 LT (Figure 2d–2f), and 1300 LT (Figures 2g–2i) for the three simulations with grid points of 96^3, 192^3, and 320^3.

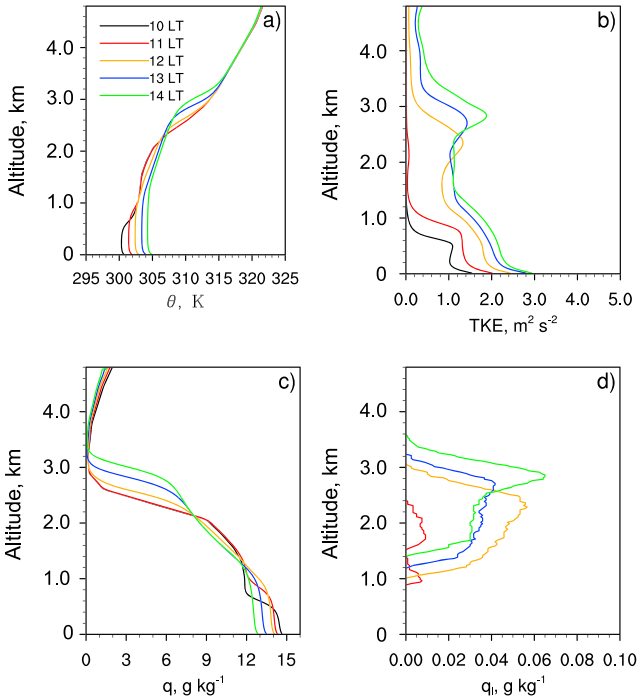

Figure 3. Horizontally averaged over the domain vertical profiles of (a) θ, (b) TKE, (c) q, and (d) q_l averaged over a 30 min period at 1000 LT, 1100 LT, 1200 LT, 1300 LT, and 1400 LT for the simulation with grid points of 192^3.

3. Results

We simulate the two scenarios (i.e., the NOAQU scenario and the AQU scenario) using the 192^3 resolution. Aqueous chemical reactions only occur in liquid water in clouds, but the effects of adding aqueous scheme can extend over the entire domain. Therefore, we analyze the changes in BVOC distributions at two scales: the first at the cloud-scale to understand the local effects of aqueous chemistry and the second at the scale of the entire domain to evaluate the larger-scale effects. Cloud-scale calculations are described in section 3.2 below. Domain-wide average vertical profiles of the mixing ratios are calculated horizontally averaged over the entire domain at each model level and represent the equivalent area of a typical regional chemistry model resolution (e.g., ~14 km).

3.1. Meteorology

For both the NOAQU and AQU simulations, the meteorological initial conditions and forcing parameters are identical, as we make no changes to the meteorology between the simulations. In the simulation, clouds continually form and dissipate beginning at 1045 LT, with a cloud fraction ranging from 0% to 47% over the course of the simulation (Figure 1b). Cloud base is at 1.5 km and the cloud top reaches 3.5 km in the early afternoon (Figure 1a), with peak cloud fractions between 1100 and 1230 LT (Figure 1b). From 1000 LT to 1400 LT, ABL development is observed through the profiles of potential temperature (θ; K) and TKE ($m^2\ s^{-2}$) (Figures 3a and 3b). The ABL height is defined as the height where a bottom-up inert tracer emitted from the surface has a horizontal model domain averaged mixing ratio that is 0.5% of its surface value (Kim et al., 2012; Vilà-Guerau de Arellano et al., 2005). The ABL height is around 1 km at 1000–1100 LT and starts to increase rapidly after 1200 LT, reaching up to 3 km at 1400 LT. In the subcloud layer, near-surface θ increases about 5 K over this time period, while θ at 3 km decreases about 5 K, leading to a less stable atmospheric environment. TKE increases with time as surface heat fluxes increase throughout the day, with the largest values in the subcloud layer and a second local maximum emerging in the cloud layer (1–3.5 km) from 12 to 14 LT. Total water specific humidity (q; $g\ kg^{-1}$) decreases near surface but increases aloft based on initial profiles provided by reanalysis and sonde data (Figure 3c). Liquid water specific humidity (q_l; $g\ kg^{-1}$) increases at 1200 LT between 1 and 3 km, matching the convective environment indicated by strong TKE at this height (Figure 3d).

3.2. Cloud Sampling

We focus on changes in the chemistry and transport of BVOC caused by introducing aqueous-phase reactions. Aqueous-phase reactions occur only in liquid water present in the cloud layer (Figure 1a). To capture these small-structure changes where clouds are present, we select a cloudy column within the model domain for analysis of the impact of aqueous chemistry. We select a vertical column with high liquid water path (LWP) based on visual inspection at a time of peak cloud fraction (1200 LT in this case), hereinafter called the "cloudy column." The LWP altitude range is from the surface to the top of the simulation domain. This column has LWP larger than 160 $g\ m^{-2}$ and is selected to highlight the detailed chemical processes occurring within clouds. This cloudy column is defined by $25 \times 25 \times 192$ grid points representing a 1,875 m ×1,875 m ×4,800 m region. The column remains spatially fixed over time; thus, clouds evolve within the column. We evaluate the vertical profile within the column by horizontally averaging over the cloudy column's horizontal extent and time averaging over 30 min intervals. To understand the temporal impacts of aqueous phase chemistry on the chemical species in the cloud layer, we evaluate aqueous chemistry in the 2–3 km altitude layer of the cloudy column and over the domain, respectively. In addition, an instantaneous vertical cross section of the LES domain that intersects with the center of the selected cloudy column is analyzed to compare and understand the meteorological versus chemical factors on BVOC mixing ratios and resulting chemistry.

Following the cloud sampling methods introduced above, we select a 30 min period at 1200 LT (1145–1215 LT) with peak cloud fraction (Figure 1a) to identify a region of the domain with high liquid water. Figure 4a

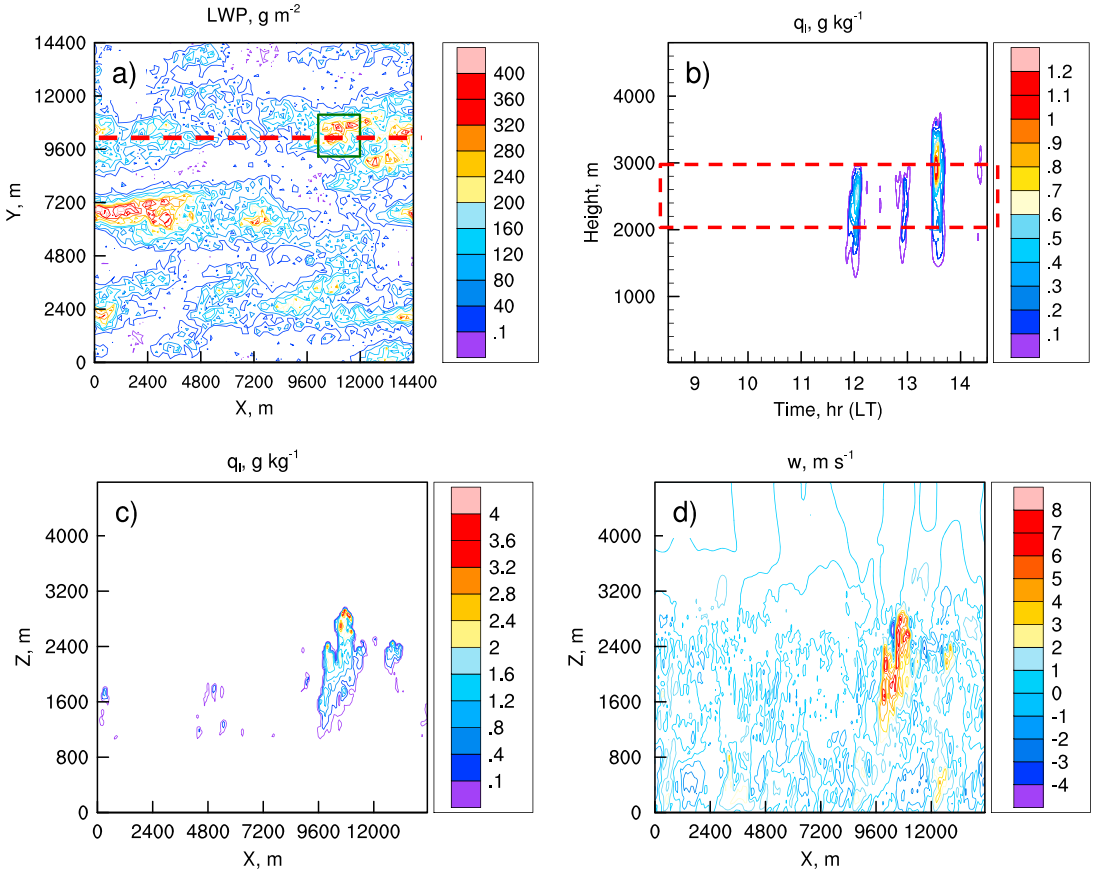

Figure 4. Horizontal contour map of LWP averaged over a 30 min period at (a) 1200 LT with a selected domain of high liquid water content ("cloudy column"; green box). (b) Temporal evolution of q_l averaged in the cloudy column is shown with the red dashed box marking the altitude range in the cloud layer (2–3 km) for averaging. (c and d) Instantaneous vertical cross sections, cutting through the center of the high liquid water column as marked by the red dashed line in Figure 4a, of q_l and w at 1200 LT.

shows the horizontal distribution of the 30 min averaged LWP centered at 1200 LT. The domain primarily has LWP less than 200 g m^{-2}, a value within the expected range for shallow cumulus clouds (e.g., Lenderink et al., 2004). A few high LWP regions are also observed in Figure 4a, indicating regions with deeper clouds and higher liquid water content. We select a region with high LWP (>240 g m^{-2}) to analyze the variations of BVOC under different phases of cloud evolution (Figure 4a; red box). The temporal evolution of q_l in this cloudy column (Figure 4b) shows temporally intermittent clouds from 1.5 km to 3.5 km altitude and therefore our analysis of BVOC temporal variations in this cloudy column focuses on the 2–3 km altitude region (Figure 4b, red dashed lines) (section 4.1).

We use an instantaneous *x-z* cross section of meteorological and chemical variables at 1200 LT to study the effects of vertical transport of liquid water on chemical constituents. The instantaneous vertical cross section of q_l shows a cloud cluster (Figure 4c) with q_l of 1.6–2.0 g kg^{-1} in the main cloud region and higher mixing ratios at the top of the cloud. The cloud cluster has strong upward motion ($w = 4$ to 7 m s^{-1}) inside the clouds (Figure 4d), and weak downdrafts observed near cloud edges.

3.3. Vertical Profiles of Chemical Species

For the AQU simulation, we investigate horizontally and 30 min averaged vertical profiles of isoprene (Figure 5a), primary isoprene oxidation products (Figures 5b–5d), and HCHO (Figure 5e), together with OH, HO_2, RO_2, NO_2, and NO (Figures 5f–5j). RO_2 is calculated as the sum of all the organic peroxy radicals in the LES chemical scheme. The mixing ratio profiles of the chemical variables display the total mixing ratio, or the sum of gas plus aqueous phase mixing ratios. The distribution of species in the ABL depends on both chemistry and turbulent mixing, and here we discuss the vertical distribution of BVOC, HO_x, and NO_x, as simulated by the LES.

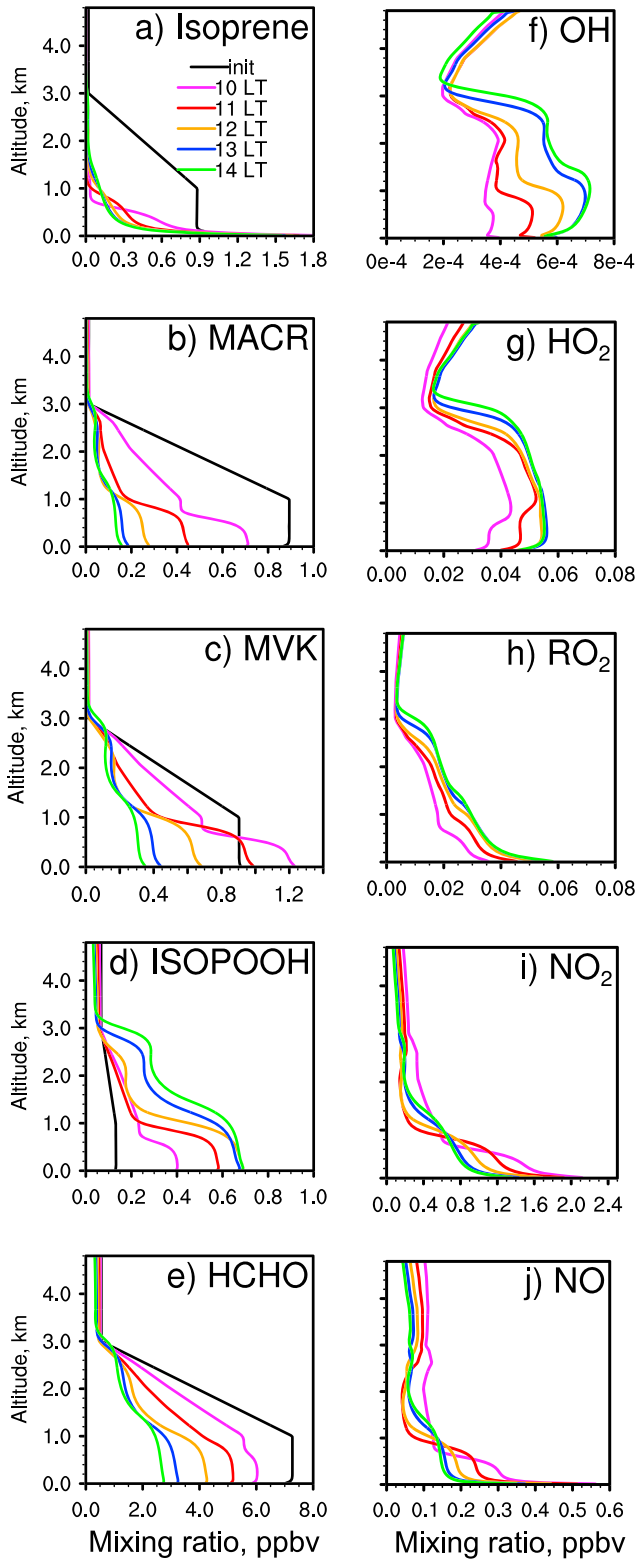

Figure 5. Horizontally averaged over the domain vertical profiles of (a) isoprene, (b) MACR, (c) MVK, (d) ISOPOOH, (e) HCHO, (f) OH, (g) HO_2, (h) RO_2, (i) NO_2, (j) NO averaged over a 30 min period at 1000 LT, 1100 LT, 1200 LT, 1300 LT, and 1400 LT for the AQU simulation, with the black lines (Figures 5a–5e) showing the initial profiles of the BVOC species.

Emitted from the surface, isoprene rapidly reacts with OH in the gas phase. Mixing ratios are highest near the emission source and then decrease rapidly with height due to chemical loss. Additionally, isoprene diminishes more rapidly with height as OH production increases through photochemical production during the day (e.g., from 1000 LT to 1400 LT). After 1100 LT, a small amount of isoprene is transported upward above cloud base (Figure 5a), due in part to the strong upward motions in clouds.

Generally, isoprene oxidation products (MACR, MVK, HCHO, and ISOPOOH) have vertical gradients with higher mixing ratios near the surface reflecting the near-surface isoprene source (Figures 5b–5e). In the morning (1000 LT) above 1 km, MACR, MVK, and HCHO mixing ratios are elevated due to the chemical initial conditions from P-3B measurements (Figures 5a–5e), representing observed oxidation products in a residual layer aloft or transported in from upwind regions. These mixing ratios are then depleted largely from 1000 LT to 1400 LT due to reactions with OH below 3 km (Figures 5b, 5c, and 5e). MACR, MVK, and HCHO have longer lifetimes than isoprene, resulting in well-mixed mixing ratios below the cloud base (~1 km). About an hour after cloud formation, the vertical profiles of MACR, MVK, and HCHO are also well mixed in the cloud layer (1–3 km) with lower mixing ratios. In contrast to the other BVOC oxidation products, ISOPOOH mixing ratios increase during the daytime. Its longer lifetime compared with the other BVOC species in Figure 5 (Li et al., 2016) allows ABL motions to transport ISOPOOH aloft beginning at 1200 LT (Figure 5d).

OH mixing ratios are mainly controlled by photochemistry; thus, its vertical profile (Figure 5f) reflects OH sources and sinks. Mixing ratios are lower near the surface (where reaction of OH and isoprene dominates) and higher aloft (details of OH sources and sinks are presented in section 4.2). As in Li et al. (2016), diurnal photolysis rates are calculated off-line with the NCAR Tropospheric Ultraviolet and Visible (TUV) Radiation Model (Madronich & Flocke, 1999), meaning that the presence of clouds in these LES simulations would not affect the photolysis rates. Kim et al. (2012) found 15% decrease in OH but negligible effect on HCHO caused by cloud scattering effects on photolysis rates, indicating that the importance of photolysis in our cloudy simulations may be overestimated for OH but should be reasonably accurate for HCHO. TUV-calculated photolysis rates peak at around 1315 LT in the simulations. Also, as the primary precursor of OH, O_3 increases past 1 pm (not shown), leading to OH increasing beyond local noon. HO_2 vertical profiles are similar to OH due to fast conversion reactions between OH and HO_2 (Figure 5g). NO_2 vertical profiles (Figure 5i) show decreasing near-surface mixing ratios and increasing upward transport from 1000 LT to 1400 LT. Atmospheric photochemical conversion between NO and NO_2 leads to a similar variation of NO vertical profiles (Figure 5j) as NO_2.

4. Effects of Aqueous Chemistry on Chemistry in the ABL

To investigate the impacts of aqueous-phase reactions on BVOC, we evaluate the two simulations with (AQU) and without (NOAQU) aqueous-phase reactions for the vertical changes of total (gas + aqueous) mixing ratios at 1200 LT and the temporal evolution within the cloud layer (2–3 km) for the cloudy column and across the entire horizontal LES domain. The changes due to aqueous chemistry in the cloudy column

reflect the effects of aqueous processes in clouds, and the domain-wide changes evaluate aqueous chemistry effects on a regional scale. Segregation between the key BVOC species and OH are also calculated and compared with prior studies.

To obtain average vertical profiles in the cloudy column, mixing ratios at each model level are horizontally averaged over the column region and temporally averaged for the 30 min time period centered on the desired time (i.e., 1145–1215 LT). Similarly, domain-wide vertical profiles are averaged horizontally over the entire LES simulation domain. To study the temporal evolution of the chemical species, their mixing ratios at each model level are horizontally averaged over the column region or the domain and then vertically averaged for all grid points spanning the 2–3 km altitude region. Spatial standard deviations are applied only on the averaged quantities related to the cloudy column, reflecting the magnitude of mixing ratio variations relative to this average over the horizontal extent of the cloudy column and the 2–3 km region at each time interval.

4.1. Temporal Evolution of In-Cloud Chemistry

We investigate the temporal variations within the 2–3 km altitude layer of the selected cloudy column (Figure 4a) and the whole domain over the time period of dominant cloud formation. In the cloudy column, three cloud clusters develop at around 1200 LT, 1300 LT, and 1330 LT (Figure 4b). Clouds lead to strong upward transport, increasing mixing ratios that correspond to q_l variation and updrafts (Figure 4d). BVOC and oxidant mixing ratios in the cloud layer change on a similar time scale as q_l, with mixing ratios of the two simulations diverging when q_l increases (Figure 6).

Prior to cloud development at 2–3 km, the isoprene mixing ratio is very low (~5 parts per trillion by volume (pptv)), similar to isoprene mixing ratios simulated by Kim et al. (2012). As clouds develop in the column, convective motion transports isoprene upward and isoprene mixing ratios increase up to 140 pptv (i.e., when $q_l > 0$ g kg^{-1}). Isoprene mixing ratios quickly decrease when clouds dissipate or exit the predefined column (Figure 6a), which is primarily due to its fast reaction with OH. When looking beyond the cloudy column to the full domain, the domain-wide averaged q_l (~0.05 g kg^{-1} peak values) is much lower than the cloudy column (~0.2–0.6 g kg^{-1} peak values) yet domain-averaged isoprene increases by about ~10 pptv at 2–3 km (Figure 6e).

MACR decreases from 1030 LT to 1130 LT before cloud formation due to its gas-phase reaction with OH and reaches 30 pptv by midday. Similar to isoprene, MACR mixing ratios increase within convective updrafts and decrease in the absence of clouds (Figure 6b). Domain-averaged MACR increases 15% in the AQU simulation as compared to the NOAQU simulation (Figure 6f). In the AQU simulation, OH reductions (Figure 6c) slow BVOC oxidation rates and increase the peak mixing ratios of isoprene and MACR slightly higher than the NOAQU simulation (Figures 6a and 6b).

The mixing ratios of OH increase from 1030 LT to 1430 LT due to photochemical production during midday (Figure 6c). In the NOAQU simulation, OH increases sharply when q_l increases, then decreases after each cloud event. In the AQU simulation, OH decreases by up to 25% of the NOAQU simulation values when q_l increases, signifying the effects of adding aqueous-phase reactions in the AQU simulation (Figure 6c and Table 1). Gas-phase chemistry also contributes to its depletion; for example, segregation of NO and HO_2 induced by their solubility differences reduces OH production in the presence of clouds. However, the gas phase contribution is much smaller than contributions from aqueous phase chemistry (discussed in section 4.2). The BVOC lifetime (according to their reaction rates with OH) is inversely proportional to the OH mixing ratio (Li et al., 2016). Therefore, the 25% OH decrease within the cloudy column in the AQU simulation leads to a 33% increase of BVOC lifetimes in clouds. Domain-averaged OH shows a smaller divergence between the AQU and the NOAQU simulations (Figure 6g), which could result from regions without the OH decrease in the AQU simulation or without the OH enhancement in the NOAQU simulation, eliminating the accumulated effects of aqueous processes. HCHO concentrations are initialized at ~2 ppbv in the 2–3 km cloud layer based on P-3B observations. However, the model lacks emissions of anthropogenic VOC that would contribute to HCHO formation; therefore, concentrations decrease between 0830 and 1145 LT. After cloud formation, HCHO shows a relatively constant mixing ratio (1.2 ppbv) when q_l decreases to zero in the NOAQU simulation (Figure 6d), indicating a balance of its photochemical sources and sinks. Adding aqueous-phase reactions (AQU simulation) decreases the HCHO mixing ratio by 0.2 ppbv (17%), due to its

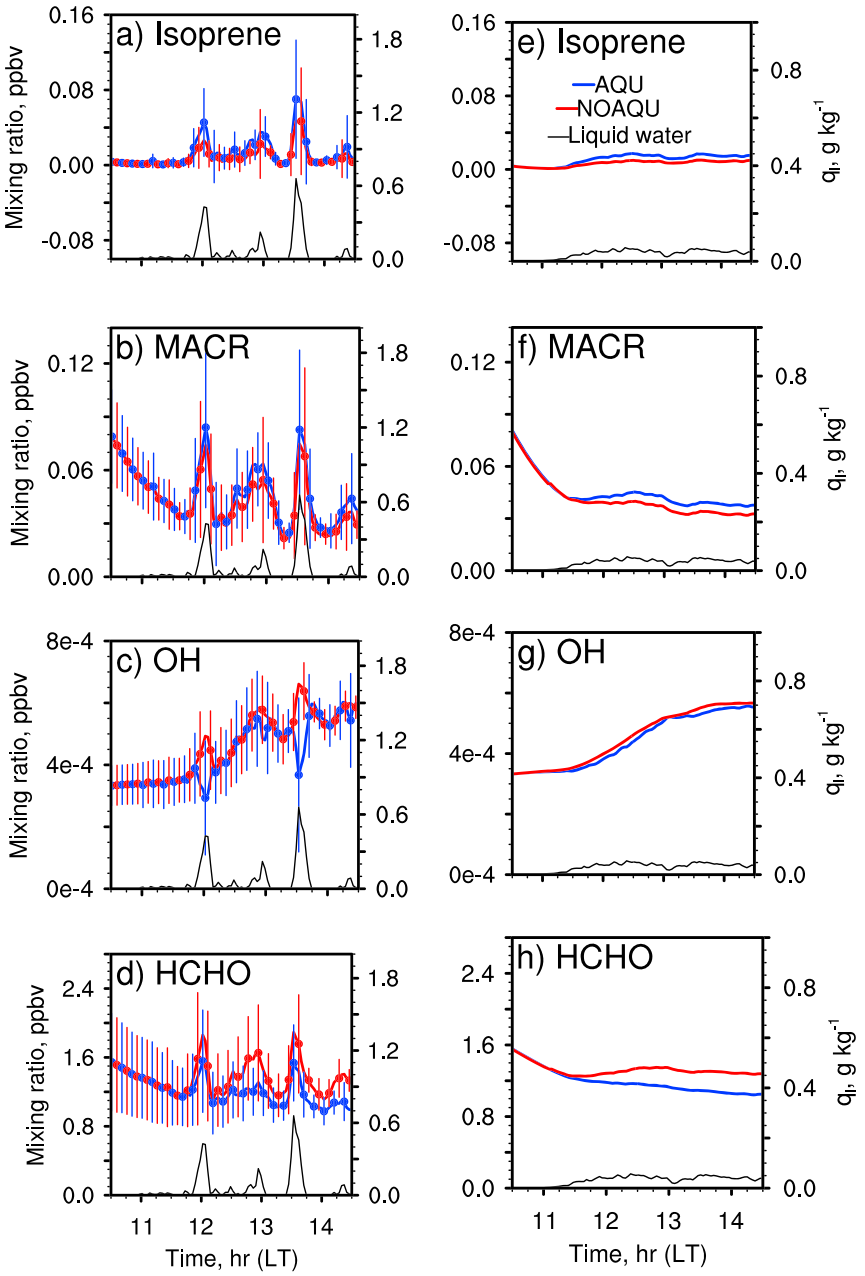

Figure 6. Temporal evolution averaged in the cloudy column (Figures 6a–6d) and over the domain width (Figures 6e–6h) of the cloud layer (2–3 km) of total (gas + liquid) (a and e) isoprene, (b and f) MACR, (c and g) OH, and (d and h) HCHO for the NOAQU (red) and AQU simulations (blue). Vertical bars (Figures 6a–6d) represent the spatial standard deviation within the cloudy column of the cloud layer (2–3 km). The liquid water mixing ratio (q_l, g kg^{-1}) is represented in black (right axis).

solubility and fast consumption by aqueous-phase OH. This reduction is similar to decreasing HCHO mixing ratios simulated with aqueous chemistry by Lelieveld and Crutzen (1991), Barth et al. (2003), and others (e.g., Chameides & Davis, 1982, Chameides, 1984, or Jacob, 1986). The lifetime of HCHO is longer than isoprene, MACR and OH (Li et al., 2016); therefore, aqueous chemistry could also have an accumulated effect on HCHO variation. Including aqueous-phase processes not only decreases HCHO when clouds exist but also steadily decreases mixing ratios in the cloud layer over the course of the simulation. Domain-wide HCHO variations also show an accumulated effect of aqueous processes, with an 18% decrease in the AQU simulation compared to the NOAQU simulation at 1430 LT (Figure 6h). Compared with the updated chemical mechanism with both gas- and aqueous-phase reactions, this suggests that gas-phase only

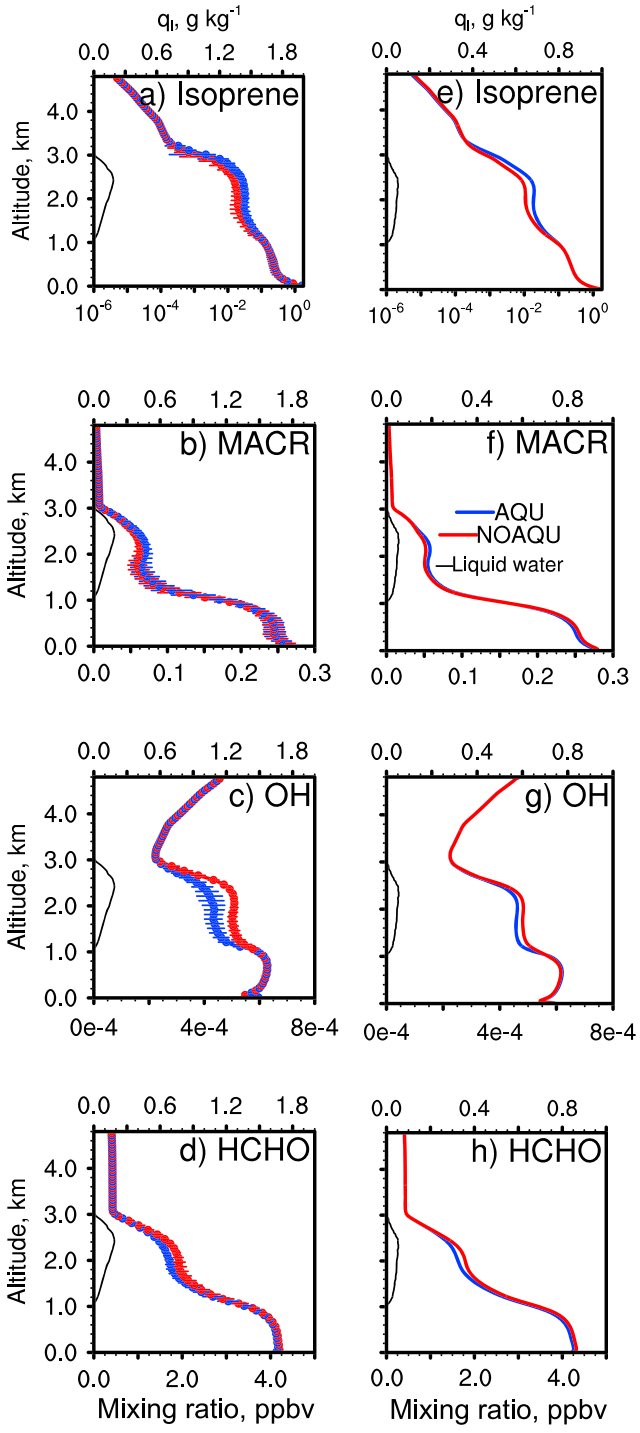

Figure 7. Vertical profiles horizontally averaged over the cloudy column (Figures 7a–7d) (marked in Figure 4a) and over the domain width (Figures 7e–7h) of (a and e) isoprene, (b and f) MACR, (c and g) OH, and (d and h) HCHO averaged over a 30 min period at 1200 LT for the NOAQU (red) and AQU simulations (blue). Horizontal bars (Figures 7a–7d) represent the spatial standard deviation within the cloudy column. q_l (g kg^{-1}) is represented in black (top axis).

mechanisms may overestimate HCHO by about 18% in the early afternoon during convective cloud events. We note that anthropogenic emissions are not included in these simulations, which could affect the magnitude of in-cloud HCHO changes.

ISOPOOH shows an increasing trend over time (not shown), signifying an accumulation of this BVOC oxidation product in the cloud layer due to its longer lifetime than isoprene, MACR, MVK, and the HO_x species (Li et al., 2016). No difference between the two simulations is observed for the ISOPOOH time series (Figure 6g), indicating that aqueous chemistry does not affect ISOPOOH mixing ratios. We note that ISOPOOH is treated as slightly soluble in the LES. We use a deposition velocity of 0.909 cm s^{-1} for ISOPOOH in the simulations, which is lower than the deposition velocity of 1.5 ± 0.4 cm s^{-1} used by Wolfe et al. (2015) for ISOPOOH+ isoprene dihydroxyepoxides (IEPOX). Compared with the NOAQU simulation, NO_x mixing ratios are enhanced in the AQU simulation (not shown) as a result of decreased HO_x.

4.2. Aqueous Chemistry Effects on Vertical Profiles of Chemical Species

Vertical profiles of total (gas plus aqueous) mixing ratios of key BVOC species, oxidation products, and oxidants horizontally averaged reveal differences between the two simulations in the cloudy ($q_l > 0$ g kg^{-1}) layer from 1 to 3 km (Figure 7). In the cloudy column (Figures 7a–7d), isoprene mixing ratios increase about 20 pptv in the cloud layer (1–3 km) when aqueous chemistry is included (Figure 7a). In addition, MACR increases 15 pptv (about 20%; Figure 7b) and mixing ratios of OH and HCHO decrease up to 20–25% due to the aqueous-phase reactions (Figures 7c and 7d). As was shown with the temporal evolution of HCHO (Figure 6d), aqueous-phase chemistry depletes HCHO and reduces HCHO mixing ratios in the cloudy column by 20% compared to gas-phase only chemistry (Figure 7d). Compared with the cloudy column, domain-wide average profiles show smaller changes in the chemical species between the AQU and the NOAQU simulations (Figures 7e–7h), with about a 14% increase for MACR, 18% decrease for OH, and 18% decrease for HCHO.

To understand the effects of aqueous chemistry on the key chemical species, we focus on the cloudy column where the impacts are the greatest. The decrease of OH with the addition of aqueous chemistry mainly results from the rapid oxidation of HCHO in clouds (Figure 8). In the NOAQU simulation, OH is chemically produced through reactions of HO_2 and NO, and O_3 photolysis (Figure 8a) and is depleted primarily through reaction with CO and HCHO (Figure 8b). Compared with the total (sum of aqueous- and gas-phase) production and loss rates in the NOAQU simulation (Figures 8a and 8b), the total OH production rate increases slightly (about 5%) in the cloud layer in the AQU simulation, and the total loss rate increases about 30% on average (Figures 8c and 8d), leading to a net loss in OH production. While the aqueous-phase $O_3 + HO_2$ reaction is an important pathway that increases the OH production in the cloudy column (about 10%) (Figure 8c), it is offset by the aqueous HCHO oxidation with OH, which is the dominant loss pathway for OH and contributes more than 90% of the change in the OH loss in the cloud layer. This is followed by the aqueous-phase reaction of OH and CH_3OH, which contributes about 30% of the change in the OH loss (Figure 8d), although we note that the high mixing ratios of CH_3OH (~6.5 ppbv measured by P-3B in the ABL) at the Fair Hill site in the 2011 DISCOVER-AQ campaign contribute to

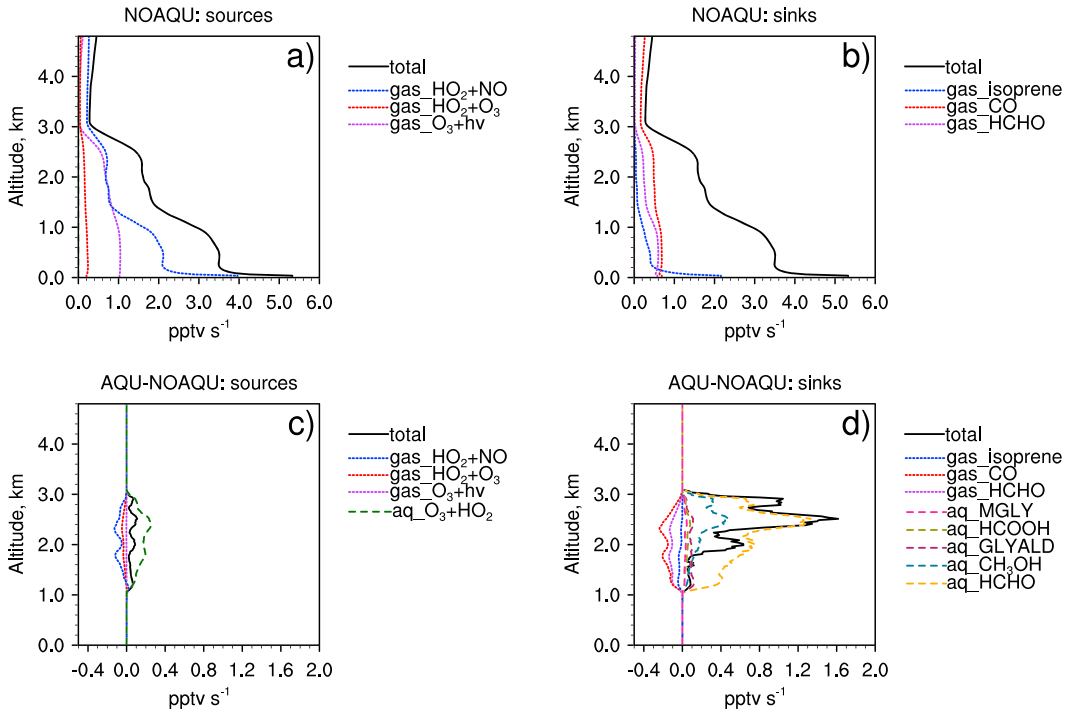

Figure 8. Horizontally averaged over the cloudy column production (Figure 8a) and loss rates (Figure 8b) of OH in the cloudy column at 1200 LT for the (a and b) NOAQU simulation, and (c and d) the changes (AQU-NOAQU) in the production (Figure 8c) and loss rates (Figure 8d) after including aqueous phase chemistry in the AQU simulation.

the importance of this reaction in the budget. Other primary loss pathways for OH are the aqueous-phase reactions of OH and GLYALD, OH and HCOOH, and OH and MGLY, contributing about 8%, 5%, and 2% of the change in the OH loss in the cloud layer, respectively (Figure 8d). These results for OH sources and losses are qualitative only, because the LES model was configured such that Henry's law equilibrium is used to estimate OH aqueous-phase concentrations, resulting in higher OH aqueous-phase concentrations than found by other models (e.g., Tilgner et al., 2013). HO_2 dissolves in the aqueous phase more easily than OH, which further suppresses gas-phase reactions that reform OH (Chameides & Davis, 1982). For example, the OH production rate through the reaction of HO_2 and NO decreases by about 10% in the AQU simulation (Figure 8c) compared with that in the NOAQU simulation (Figure 8a). These results suggest that the lack of aqueous-phase reactions could overestimate OH in the cloud layer. We note that because aqueous chemistry changes the vertical gradient of each species, turbulent transport may also play a role in decreasing OH; however, this term contributes less than 1% to the OH decrease (not shown) and is therefore small compared to aqueous HCHO oxidation.

Decreased oxidants lower the reaction rates of the BVOC chemistry, resulting in increased mixing ratios of isoprene and its primary oxidation products (e.g., MVK and MACR). ISOPOOH has a longer lifetime (2.7 hr with respect to OH gas-phase oxidation, Li et al., 2016) than other species like MACR and MVK and is only slightly soluble in the aqueous phase. ISOPOOH mixing ratios are similar in the two simulations (not shown), reflecting the lack of aqueous-phase reaction of ISOPOOH and the similar gas-phase net production rates of ISOPOOH calculated under both scenarios (Figure S1 in the supporting information). In addition, we note the difference in cloud fraction ($<$10%) between the 192^3 and 320^3 simulations after 1200 LT. The 320^3 simulation simulates a slightly higher cloud fraction, indicating using a higher resolution (320^3) could lead to a minor increase ($<$1%) in the differences of the vertical profiles and the temporal evolutions of the key chemical species between the NOAQU and AQU simulations over the entire domain.

4.3. Segregation

Understanding chemical production and loss rates is crucial to interpret the oxidation and vertical distribution of the BVOC species. However, these chemical reactions are influenced by turbulent eddies of all

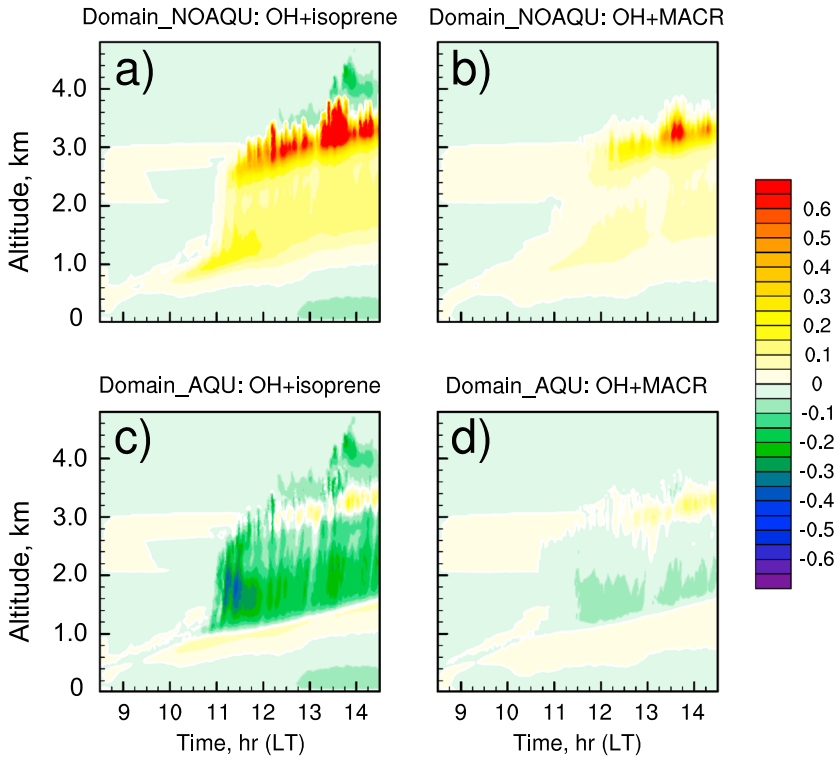

Figure 9. Temporal evolution of I_s over the domain for (a and c) OH + isoprene and (b and d) OH + MACR for the NOAQU (Figures 9a and 9b) and AQU (Figures 9c and 9d) simulations.

scales. Numerical models that do not resolve turbulence typically ignore the effects of turbulent mixing by assuming constituents are well mixed. The LES resolves the energy-containing turbulent scales of motion thereby permitting investigation of the effects of insufficient mixing on chemical production and loss rates.

We calculate the intensity of segregation (I_s) between OH and the BVOC species to study the impact of aqueous-phase chemistry on turbulence-induced modification to their overall reaction rate. I_s is calculated as:

$$I_s = \frac{\overline{\mathrm{VOC}_i' \mathrm{OH}'}}{\overline{\mathrm{VOC}_i}\ \overline{\mathrm{OH}}}, \tag{1}$$

which is the covariance between a BVOC species and OH $\left(\overline{\mathrm{VOC}_i' \mathrm{OH}'}\right)$, where the overbar represents a horizontal average across the entire LES domain and the $'$ represents a deviation from that average) divided by the product of the horizontally averaged BVOC ($\overline{\mathrm{VOC}_i}$) and OH ($\overline{\mathrm{OH}}$). Negative I_s indicates a reduction in the reaction rate due to segregation of the reactants and positive I_s represents an increase in the reaction rate (Karl et al., 2007; Li et al., 2016; Molemaker & Vilà-Guerau de Arellano, 1998; Verver et al., 1997).

We calculate I_s for OH and isoprene, and for OH and MACR over the entire LES domain for the two simulations at each time step. Because a cloud fraction larger than 30% is maintained in the domain after cloud formation (Figure 1b), continuous positive or negative I_s values are calculated in the cloud layer (Figure 9). In the NOAQU simulation, positive I_s values in the cloud layer (Figures 9a and 9b) indicate higher reaction rates between OH and the BVOC species than one would predict in the absence of turbulence consistent with Ouwersloot et al. (2011) analysis of OH-isoprene segregation. Strong positive I_s occurs near or above the top of the clouds (Figures 9a and 9b). The positive correlations are predominantly due to chemical transformations (Figure 10a) leading to the very low mixing ratios of these species in the free troposphere (Figure 5), which will be further discussed below using the covariance budget. In our case with nonprecipitating clouds, adding aqueous-phase chemistry leads to a decrease in the reaction rates of OH and isoprene by about 20–40%, consistent with an up to 39 ± 7% reduction of the isoprene-OH reaction rate in the cloud layer observed by Karl et al. (2007), and OH and MACR by about 10% in the cloud layer over the domain. We note the relatively low mixing ratios of isoprene at this altitude (Figure 7a), suggesting that the impact of the isoprene-OH

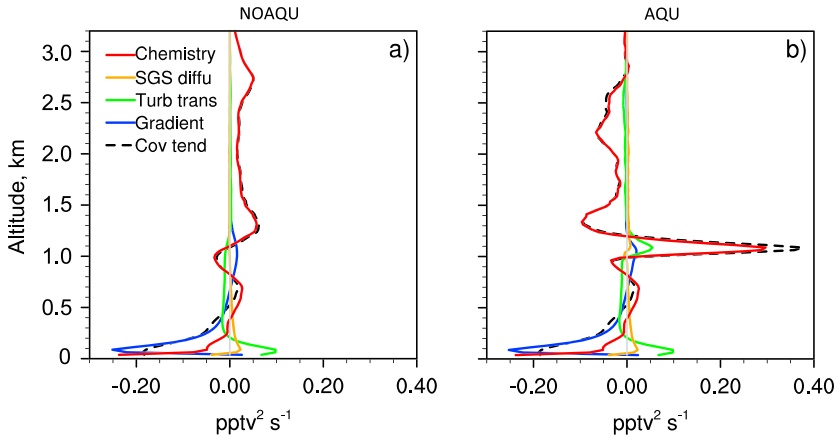

Figure 10. Horizontally averaged over the domain vertical profiles of covariance budget (black dashed line), including the sum of two gradient terms (blue), a turbulent transport term (green), the sum of two subgrid-scale diffusion terms (orange), and a chemistry term (red), averaged over a 30 min period at 1200 LT for the (a) NOAQU and (b) AQU simulations. The gray line marks the zero value.

segregation should not significantly change peroxy radical production at this altitude. In the AQU simulation, the reactions of OH and MVK, OH and MGLY, OH and ACETALD, and NO and HO_2 also exhibit negative I_s in the cloud layer over the domain (Figure S2). The impacts of turbulence on the reaction rates of OH and MVK, OH and MGLY, and NO and HO_2 are comparable spatially but weaker in magnitude (5–10%) than on the reaction of OH and MACR, and the impact on reaction rate of OH and ACETALD is minor (<5%).

To understand the processes controlling segregation between isoprene and OH in the modeling domain, we calculate the covariance budget as follows:

$$\partial\left\langle \overline{(C_5H_8)'(OH)'}\right\rangle/\partial t = -\left\langle \overline{w'(C_5H_8)'}\,\partial\overline{(OH)}/\partial z\right\rangle - \left\langle \overline{w'(OH)'}\,\partial\overline{(C_5H_8)}/\partial z\right\rangle - \partial\left\langle \overline{w'(C_5H_8)'(OH)'}/\partial z\right\rangle$$
$$-\left\langle \overline{(C_5H_8)'(\partial\tau_{wOH}/\partial z)}\right\rangle - \left\langle \overline{(OH)'(\partial\tau_{wC_5H_8}/\partial z)}\right\rangle + \partial\left\langle \overline{(C_5H_8)'(OH)'}\right\rangle/\partial t|_{chem} \quad (2)$$

where $'$ indicates deviation from the horizontal average, the overline denotes horizontal average, angle brackets denote the time average, and τ_{wOH} and $\tau_{wC_5H_8}$ denote the subgrid stress for OH and C_5H_8, respectively (Kim et al., 2004; Moeng & Sullivan, 1994). The term on the left hand side is the tendency of covariance between isoprene and OH, while the terms on the right-hand side show how this covariance is generated. The first two terms on the right-hand side are the gradient production of the covariance between isoprene and OH, the third term represents the turbulent transport of the two species, and the fourth and fifth terms are SGS diffusion terms (Schumann, 1989; Vinuesa & De Arellano, 2003). The last term on the right-hand side is the net production/destruction of covariance from chemical transformations, which is calculated as the residual of the covariance budget.

The covariance budget is important in understanding the processes controlling segregation. Figure 10 shows the profiles of the budget terms horizontally averaged over the model domain at 1200 LT under the NOAQU and AQU simulations. In the NOAQU simulation, gradient production enhances the covariance of isoprene and OH below the cloud base (around 1 km), while turbulent transport increases the covariance near surface (below 0.2 km) (Figure 10a). The chemical reaction term also increases the covariance near surface, indicating an increase in segregation. Because of the rapid chemistry near the surface, SGS chemistry may be important to the isoprene-OH segregation (Vinuesa et al., 2006; Vinuesa & Porté-Agel, 2005), but SGS chemistry is currently neglected. The SGS diffusion term in the NOAQU simulation shifts from negative to positive below 0.5 km, with a relatively small contribution to the covariance budget. In the cloud layer (around 1–3 km), chemistry becomes the main contributor to the covariance budget, while other terms are all negligible (Figure 10a).

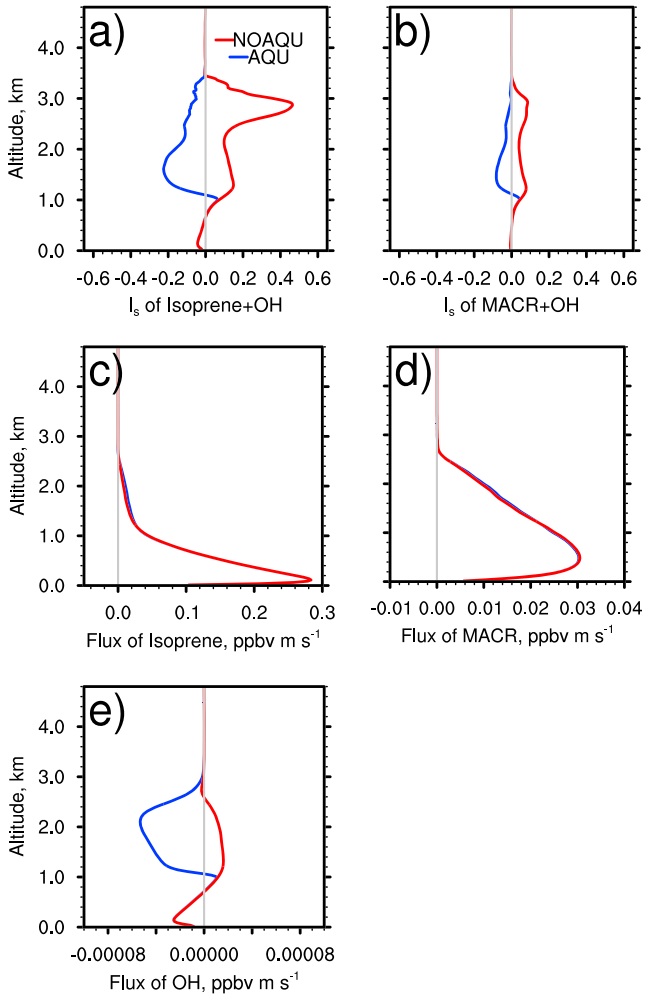

Figure 11. Horizontally averaged over the domain vertical profiles of I_s for (a) isoprene and OH, (b) MACR and OH, and (c–e) fluxes of isoprene, MACR and OH averaged over a 30 min period at 1200 LT for the NOAQU and AQU simulations. The gray lines mark the zero values of I_s and fluxes.

The contributions of the different budget terms are similar below the cloud base (around 1 km) between the two scenarios (Figures 10a and 10b). At cloud base in AQU, there is a strong increase in the contributions from chemistry and turbulent transport (Figure 10b), matching the positive I_s values at the cloud base at around 1200 LT (Figure 9c). Positive I_s results from the positive covariance between gas-phase OH and isoprene mixing ratios at that height, due primarily to the strong upward motions in clouds. In the cloud layer (around 1–3 km), chemistry drives a positive correlation in the NOAQU simulation (Figure 10a) but increases segregation in the AQU simulation (Figure 10b), which supports our previous discussion regarding the importance of including aqueous-phase reactions in sections 4.1 and 4.2. The covariance budget is also calculated at 1330 LT, and the results are similar to the budget calculated at 1200 LT (not shown).

Based on the importance of chemistry in cloud layers, we further investigate the profiles of I_s for reactions of isoprene and OH, MACR, and OH, and their fluxes averaged over the entire horizontal domain and over a 30 min period at 1200 LT for the two scenarios (Figure 11). The magnitude of segregation in the cloud layer is similar between the NOAQU and AQU simulations, but with opposite sign (Figures 11a and 11b). While the OH chemical lifetime is estimated to be very short (~1 s in the gas phase), it is likely that OH survives in the atmosphere longer than one might expect from solely a chemistry perspective because of turbulence-induced segregation of reactants (i.e., insufficient mixing as quantified by I_s); an effect which results in a vertical flux of OH despite its short chemical lifetime. Resolved vertical flux profiles of isoprene and MACR are similar between the two simulations (Figures 11c and 11d), yet there is a large decrease in the vertical flux of OH in the cloud layer due to its aqueous chemistry (dominated by HCHO) (Figure 11e). This suggests that the loss of OH through aqueous chemistry is the dominant driver of the change in the sign of segregation in the cloud layer.

Instantaneous vertical cross sections of OH and isoprene under the two scenarios (Figure S3) also show the importance of changes in OH on the segregation in clouds. Consistent with the liquid water vertical cross section (Figure 4c), OH mixing ratios in clouds are higher than the surrounding atmosphere in the NOAQU simulation. In the AQU simulation, OH mixing ratios decrease within the cloud cluster. Vertical motion within the cloud transports isoprene upward under both scenarios, but in the AQU simulation isoprene mixing ratios are slightly higher due to aqueous reactions that consume substantial OH. While strong segregation between isoprene and OH in the cloud layer reduces reaction rates by 20–40%, the low isoprene mixing ratios in the cloud layer ($<$ 0.10 ppbv) indicate that this will likely not significantly decrease the overall chemical loss rate of isoprene in the ABL.

In this study, the LES with aqueous chemistry simulated segregation reduces reaction rates of isoprene and OH by about 10% near the surface, and by about 20–40% in the cloud layer. Ouwersloot et al. (2011) simulated similar near-surface segregation for isoprene and OH (10%) with homogeneous surface emission and found an up to 20% reduction in isoprene-OH reaction rates with heterogeneous surface emissions. Radiation also plays a role in modifying chemical reactions. Barth et al. (2002) found that O_3 depletion was enhanced (by 3%) with the radiative effect, and this enhancement was much stronger for HO_x species with short lifetimes. Vilà-Guerau de Arellano et al. (2005) found that radiation scattering by clouds affects photolysis rates, with a substantial effect (10–40%) locally, and also pointed out that this effect was more important for short-lived chemical species. Kim et al. (2012) further studied the impact of cloud shading on isoprene emissions and found that while the inclusion of cloud-modified photolysis frequencies increased the

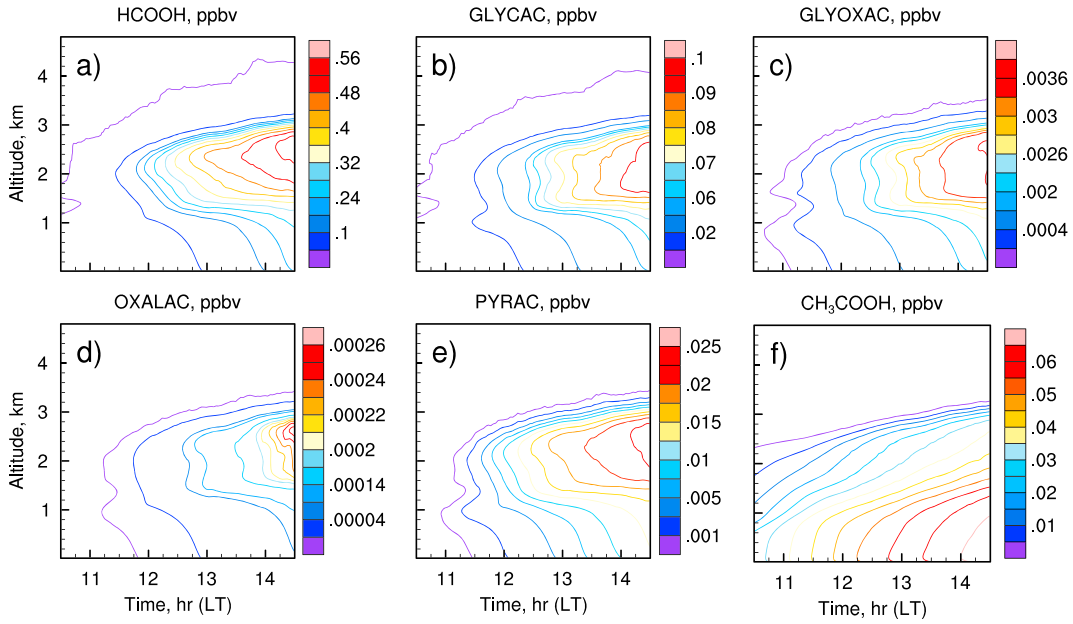

Figure 12. Temporal evolution of horizontally averaged over the domain (a) HCOOH, (b) GLYCAC, (c) GLYOXAC, (d) OXALAC, (c) PYRAC, and (f) CH_3COOH for the AQU simulation.

subcloud isoprene (>10%), this increase was canceled when including cloud-induced isoprene emission reduction. These effects of cloud-modified photolysis rates were confirmed in a global scale as well (Tie et al., 2003). Kim et al. (2016) found the change in reaction rate also depended on environmental NO_x mixing ratios, with 17–23% reduction of reaction rate for isoprene + OH in high NO_x conditions (~10 ppbv of NO_x in the boundary layer), and 6–14% reduction in low NO_x conditions (0.1–0.3 ppbv NO_x). These uncertainties of surface conditions, chemical mechanisms, emissions uncertainties, and the alteration of photolysis rates by clouds are known to influence BVOC reaction rates at a similar magnitude. This work quantifies the chemistry-turbulence interaction rate under convective conditions, which improves our understanding of effects of chemistry and mixing on key chemical species.

4.4. Formation and Transport of Organic Acids

The addition of aqueous phase reactions from Table 1 introduces the formation of aqueous-phase organic acids. In the model, acetic acid (CH_3COOH) is formed by both gas- and aqueous-phase reactions. All other organic acids are formed exclusively in the aqueous phase. No organic acid measurements were available during 2011 DISCOVER-AQ campaign. For the acids (e.g., HCOOH, GLYCAC, GLYOXAC, OXALAC, and PYRAC) form only through aqueous-phase reactions in the LES chemical mechanism, their mixing ratios are zero in the NOAQU simulation. Once formed in the aqueous phase, they can be oxidized by OH and H_2O_2. The remaining acids enter the gas phase as liquid cloud water evaporates, thereby influencing mixing ratios in both phases. The dominant organic acids are HCOOH, which is mainly formed through the aqueous OH oxidation of HCHO, and GLYCAC (Figure 12), which is produced by the OH oxidation of a third-generation isoprene oxidation product GLYALD (Table 1). Other acids formed in the mechanism are GLYOXAC (produced from the OH oxidation of CHOCHO) and PYRAC and OXALAC, formed from MGLY (Table 1).

Mixing ratios of these organic acids averaged over the simulation domain increase gradually in the cloud layer (2–3 km) after clouds develop at about 1030 LT (Figure 1). The organic acids accumulate over the afternoon and are mixed down toward the surface by turbulence resulting in a gradual increase of near-surface mixing ratios. Due to fast turbulence mixing with a turnover time of the ABL of ~13 min (Li et al., 2016), near-surface mixing ratios reach about 20% of the mixing ratios in the cloud layer within 1 h after cloud formation, which occurs at around 1200 LT when the first cloud cluster develops (Figure 4b). The mixing ratios of HCOOH, GLYCAC, GLYOXAC, OXALAC, and PYRAC in the cloud layer then increase to 560 pptv, 100 pptv, 3.9 pptv, 0.26 pptv, and 25 pptv at 1430 LT, with their near-surface mixing ratios reaching up to 320 pptv, 70 pptv, 2.5 pptv, 0.15 pptv, and 10 pptv, respectively, eventually reaching about 50% of their

mixing ratios in the cloud layer. Acetic acid (CH_3COOH) shows a vertical gradient, with high mixing ratios near the surface where isoprene is emitted, increasing to 70 ppbv at 1430 LT. There are only a few field experiments with measurements of formic and/or acetic acid. The studies by Paulot et al. (2011) and Millet et al. (2015) composited the results for different field experiments, averaging observations from days with different types of weather and binned the data into fairly coarse vertical resolution. Thus, direct comparison between our results and these previous studies are not possible. Chapman et al. (1995) show vertical profiles of HCOOH and CH_3COOH for one aircraft profile conducted over the northwest Atlantic, revealing elevated layers of formic and acetic acids. The mixing ratios predicted by the LES in the cloud layer are consistent with the Millet et al. (2015) study but are smaller than those observed by Chapman et al. (1995), suggesting missing gas-phase sources in the LES model of these acids. In addition, we suggest that future studies should more extensively investigate the role of clouds on the vertical distribution of organic acids. Overall, the LES results suggest that organic acids that are formed in clouds can mix within the boundary layer on the time scale of 1 h (Figure 12), indicating the importance of convection and turbulence in understanding the formation and fate of these compounds.

5. Conclusions

In this study, we investigate the impacts of cloud aqueous processes on the chemistry and transport of BVOC using a LES model with an updated chemical mechanism including both gas- and aqueous-phase reactions. We design the experiments based on a meteorological case with a diurnal pattern of nonprecipitating cumulus clouds from the Baltimore-Washington area DISCOVER-AQ campaign (Li et al., 2016). We test three mesh resolutions in the LES and find acceptable convergence of the meteorological profiles with the 192^3 mesh resolution with 25 m grid height. Using this resolution, we simulate two scenarios with and without aqueous-phase reactions to understand the importance of including aqueous-phase reactions in the boundary layer in BVOC-dominated environments.

In cloud-dominated regions with no aqueous chemistry (NOAQU simulation), mixing ratios of all chemical species increase inside the cloud compared to outside the cloud, indicating the importance of convection in transporting surface-emitted species or species produced near the surface to regions aloft. Including aqueous chemical reactions (AQU simulations) decreases HCHO up to 18% over the domain due to its solubility and the aqueous-phase oxidation by OH, which subsequently results in consumption of the HO_x species. These results suggest that omitting aqueous-phase reactions in the chemical mechanism could overestimate HO_x and HCHO in the cloud layer. As a result of decreasing HO_x, mixing ratios of isoprene and MACR increase over the domain (100% and 15%, respectively) in the cloud layer when aqueous-phase reactions are included in the chemical mechanism.

Turbulence-resolving simulation (e.g., LES) provides information on whether reactants are well mixed or segregated, which affects reactivity in the ABL. Aqueous-phase chemistry changes the sign of the covariance between BVOC (e.g., isoprene) and OH from positive to negative, producing segregation between BVOC and OH and therefore slower effective reaction rates. We find that aqueous chemistry can increase the intensity of segregation between OH and the BVOC species by up to 20–40% for the isoprene-OH reaction and 10% for MACR-OH reaction. Analysis of the covariance budget shows that the strong segregation in clouds is mainly driven by the chemical reactivity term, triggered by the decrease in OH through aqueous phase consumption.

Organic acids, noted SOA precursors formed in clouds via aqueous reactions, are included in the LES chemical mechanism. Our simulations show that these acids accumulate as the afternoon and cloud conditions progress. Turbulent mixing leads to enhanced near-surface mixing ratios of organic acids, reaching about 20% of the mixing ratios in the cloud layer within 1 h after cloud formation, with the percentages increasing up to 50% at the end of the simulation (1430 LT). We note that the spatial and temporal extents of the previous observations (e.g., in Millet et al., 2015 and Paulot et al., 2011) for organic acids are not comparable to the short-term LES simulations. In this study, missing gas-phase production of these organic acids in the LES could lead to differences in simulated vertical gradients.

Overall, this study quantifies the effect of aqueous chemistry on gas-phase chemistry and reactivity for a particular set of initial conditions and forcing. We emphasize that the conclusions presented are based on

LES simulations with homogeneous surface conditions and a simplified emission inventory without anthropogenic VOC emissions. Heterogeneous surface emissions for isoprene, the inclusion of anthropogenic VOC, and representing higher order VOC chemistry require further exploration.

Acknowledgments
This research is supported by NASA Earth and Space Science Fellowship (NESSF) NNX13AN76H and the Barbour Scholarship at the University of Michigan. The National Center for Atmospheric Research is sponsored by the National Science Foundation. We gratefully acknowledge the NCAR Graduate Visitor Program for supporting the collaboration and the development of the NCAR LES model. Data from model runs in this paper have been archived and are available through https://deepblue.lib.umich.edu/data/concern/generic_works/6w924b86j?locale=en.

References

Atkinson, R. (2000). Atmospheric chemistry of VOCs and NOx. *Atmospheric Environment*, *34*(12–14), 2063–2101. https://doi.org/10.1016/S1352-2310(99)00460-4

Barth, M., Bela, M., Fried, A., Wennberg, P., Crounse, J., Clair, J. S., … Brune, W. (2016). Convective transport and scavenging of peroxides by thunderstorms observed over the central US during DC3. *Journal of Geophysical Research: Atmospheres*, *121*(8), 4272–4295. https://doi.org/10.1002/2015JD024570

Barth, M., Sillman, S., Hudman, R., Jacobson, M., Kim, C. H., Monod, A., & Liang, J. (2003). Summary of the cloud chemistry modeling intercomparison: Photochemical box model simulation. *Journal of Geophysical Research*, *108*(D7), 4214. https://doi.org/10.1029/2002JD002673

Barth, M. C., Hess, P. G., & Madronich, S. (2002). Effect of marine boundary layer clouds on tropospheric chemistry as analyzed in a regional chemistry transport model. *Journal of Geophysical Research*, *107*(D11), AAC 7-1-AAC 7-12. https://doi.org/10.1029/2001JD000468

Barth, M. C., Kim, S.-W., Wang, C., Pickering, K. E., Ott, L. E., Stenchikov, G., … Telenta, B. (2007). Cloud-scale model intercomparison of chemical constituent transport in deep convection. *Atmospheric Chemistry and Physics*, *7*(18), 4709–4731. https://doi.org/10.5194/acp-7-4709-2007

Barth, M. C., Stuart, A. L., & Skamarock, W. C. (2001). Numerical simulations of the July 10, 1996, stratospheric-tropospheric experiment: Radiation, aerosols, and ozone (STERAO)-deep convection experiment storm: Redistribution of soluble tracers. *Journal of Geophysical Research*, *106*(D12), 12,381–12,400. https://doi.org/10.1029/2001JD900139

Berg, L., Shrivastava, M., Easter, R., Fast, J., Chapman, E., Liu, Y., & Ferrare, R. (2015). A new WRF-Chem treatment for studying regional-scale impacts of cloud processes on aerosol and trace gases in parameterized cumuli. *Geoscientific Model Development*, *8*(2), 409–429. https://doi.org/10.5194/gmd-8-409-2015

Betts, A. (1973). Non-precipitating cumulus convection and its parameterization. *Quarterly Journal of the Royal Meteorological Society*, *99*(419), 178–196. https://doi.org/10.1002/qj.49709941915

Blando, J. D., & Turpin, B. J. (2000). Secondary organic aerosol formation in cloud and fog droplets: A literature evaluation of plausibility. *Atmospheric Environment*, *34*(10), 1623–1632. https://doi.org/10.1016/S1352-2310(99)00392-1

Bower, K., Choularton, T., Gallagher, M., Colvile, R., Beswick, K., Inglis, D., … Berg, O. (1999). The great dun fell experiment 1995: An overview. *Atmospheric Research*, *50*(3-4), 151–184. https://doi.org/10.1016/S0169-8095(98)00103-3

Carlton, A. G., Turpin, B. J., Altieri, K. E., Seitzinger, S., Reff, A., Lim, H.-J., & Ervens, B. (2007). Atmospheric oxalic acid and SOA production from glyoxal: Results of aqueous photooxidation experiments. *Atmospheric Environment*, *41*(35), 7588–7602. https://doi.org/10.1016/j.atmosenv.2007.05.035

Carlton, A. G., Turpin, B. J., Altieri, K. E., Seitzinger, S. P., Mathur, R., Roselle, S. J., & Weber, R. J. (2008). CMAQ model performance enhanced when in-cloud secondary organic aerosol is included: Comparisons of organic carbon predictions with measurements. *Environmental Science & Technology*, *42*(23), 8798–8802. https://doi.org/10.1021/es801192n

Carmichael, G. R., & Peters, L. K. (1986). A second generation model for regional-scale transport/chemistry/deposition. *Atmospheric Environment (1967)*, *20*(1), 173–188. https://doi.org/10.1016/0004-6981(86)90218-0

Chameides, W. L. (1984). The photochemistry of a remote marine stratiform cloud. *Journal of Geophysical Research*, *89*(D3), 4739–4755. https://doi.org/10.1029/JD089iD03p04739

Chameides, W. L., & Davis, D. D. (1982). The free radical chemistry of cloud droplets and its impact upon the composition of rain. *Journal of Geophysical Research*, *87*(C7), 4863–4877. https://doi.org/10.1029/JC087iC07p04863

Chang, J., Brost, R., Isaksen, I., Madronich, S., Middleton, P., Stockwell, W., & Walcek, C. (1987). A three-dimensional Eulerian acid deposition model: Physical concepts and formulation. *Journal of Geophysical Research*, *92*(D12), 14,681–14,700. https://doi.org/10.1029/JD092iD12p14681

Chapman, E. G., Gustafson, W. Jr., Easter, R. C., Barnard, J. C., Ghan, S. J., Pekour, M. S., & Fast, J. D. (2009). Coupling aerosol-cloud-radiative processes in the WRF-Chem model: Investigating the radiative impact of elevated point sources. *Atmospheric Chemistry and Physics*, *9*(3), 945–964. https://doi.org/10.5194/acp-9-945-2009

Chapman, E. G., Kenny, D. V., Busness, K. M., Thorp, J. M., & Spicer, C. W. (1995). Continuous airborne measurements of gaseous formic and acetic acids over the western North Atlantic. *Geophysical Research Letters*, *22*(4), 405–408. https://doi.org/10.1029/94GL03023

Chen, J., Griffin, R., Grini, A., & Tulet, P. (2007). Modeling secondary organic aerosol formation through cloud processing of organic compounds. *Atmospheric Chemistry and Physics*, *7*(20), 5343–5355. https://doi.org/10.5194/acp-7-5343-2007

Cotton, W. R., Alexander, G. D., Hertenstein, R., Walko, R. L., McAnelly, R. L., & Nicholls, M. (1995). Cloud venting—A review and some new global annual estimates. *Earth-Science Reviews*, *39*(3-4), 169–206. https://doi.org/10.1016/0012-8252(95)00007-0

Deardorff, J. (1976a). *Clear and cloud-capped mixed layers, their numerical simulation, structure and growth and parameterization*, paper presented at Seminars on the Treatment of the Boundary Layer in Numerical Weather Prediction.

Deardorff, J. (1976b). Usefulness of liquid-water potential temperature in a shallow-cloud model. *Journal of Applied Meteorology*, *15*(1), 98–102. https://doi.org/10.1175/1520-0450(1976)015%3C0098:UOLWPT%3E2.0.CO;2

Deardorff, J. (1980). Stratocumulus-capped mixed layers derived from a three-dimensional model. *Boundary-Layer Meteorology*, *18*(4), 495–527. https://doi.org/10.1007/BF00119502

Ervens, B. (2015). Modeling the processing of aerosol and trace gases in clouds and fogs. *Chemical Reviews*, *115*(10), 4157–4198. https://doi.org/10.1021/cr5005887

Ervens, B., Carlton, A. G., Turpin, B. J., Altieri, K. E., Kreidenweis, S. M., & Feingold, G. (2008). Secondary organic aerosol yields from cloud-processing of isoprene oxidation products. *Geophysical Research Letters*, *35*, L02816. https://doi.org/10.1029/2007GL031828

Ervens, B., Gligorovski, S., & Herrmann, H. (2003). Temperature-dependent rate constants for hydroxyl radical reactions with organic compounds in aqueous solutions. *Physical Chemistry Chemical Physics*, *5*(9), 1811–1824. https://doi.org/10.1039/b300072a

Ervens, B., Turpin, B. J., & Weber, R. J. (2011). Secondary organic aerosol formation in cloud droplets and aqueous particles (aqSOA): A review of laboratory, field and model studies. *Atmospheric Chemistry and Physics*, *11*(21), 11,069–11,102. https://doi.org/10.5194/acp-11-11069-2011

Fu, T.-M., Jacob, D. J., & Heald, C. L. (2009). Aqueous-phase reactive uptake of dicarbonyls as a source of organic aerosol over eastern North America. *Atmospheric Environment*, *43*(10), 1814–1822. https://doi.org/10.1016/j.atmosenv.2008.12.029

Fu, T. M., Jacob, D. J., Wittrock, F., Burrows, J. P., Vrekoussis, M., & Henze, D. K. (2008). Global budgets of atmospheric glyoxal and methylglyoxal, and implications for formation of secondary organic aerosols. *Journal of Geophysical Research*, *113*, D15303. https://doi.org/10.1029/2007JD009505

Goldstein, A. H., & Galbally, I. E. (2007). Known and unexplored organic constituents in the Earth's atmosphere. *Environmental Science & Technology*, *41*(5), 1514–1521. https://doi.org/10.1021/es072476p

Guenther, A., Karl, T., Harley, P., Wiedinmyer, C., Palmer, P. I., & Geron, C. (2006). Estimates of global terrestrial isoprene emissions using MEGAN (model of emissions of gases and aerosols from nature). *Atmospheric Chemistry and Physics*, *6*(11), 3181–3210. https://doi.org/10.5194/acp-6-3181-2006

Guenther, A., Nicholas Hewitt, C., Erickson, D., Fall, R., Geron, C., Graedel, T., … Zimmerman, P. (1995). A global model of natural volatile organic compound emissions. *Journal of Geophysical Research*, *100*(D5), 8873–8892. https://doi.org/10.1029/94JD02950

Hegg, D. A., & Hobbs, P. V. (1979). The homogeneous oxidation of sulfur dioxide in cloud droplets. *Atmospheric Environment (1967)*, *13*(7), 981–987. https://doi.org/10.1016/0004-6981(79)90008-8

Hegg, D. A., & Hobbs, P. V. (1981). Cloud water chemistry and the production of sulfates in clouds. *Atmospheric Environment (1967)*, *15*(9), 1597–1604. https://doi.org/10.1016/0004-6981(81)90144-X

Hegg, D. A., & Hobbs, P. V. (1982). Measurements of sulfate production in natural clouds. *Atmospheric Environment (1967)*, *16*(11), 2663–2668. https://doi.org/10.1016/0004-6981(82)90348-1

Herrmann, H., Hoffmann, D., Schaefer, T., Bräuer, P., & Tilgner, A. (2010). Tropospheric aqueous-phase free-radical chemistry: Radical sources, spectra, reaction kinetics and prediction tools. *Chemphyschem*, *11*(18), 3796–3822. https://doi.org/10.1002/cphc.201000533

Herrmann, H., Schaefer, T., Tilgner, A., Styler, S. A., Weller, C., Teich, M., & Otto, T. (2015). Tropospheric aqueous-phase chemistry: Kinetics, mechanisms, and its coupling to a changing gas phase. *Chemical Reviews*, *115*(10), 4259–4334. https://doi.org/10.1021/cr500447k

Horowitz, L. W., Walters, S., Mauzerall, D. L., Emmons, L. K., Rasch, P. J., Granier, C., … Brasseur, G. P. (2003). A global simulation of tropospheric ozone and related tracers: Description and evaluation of MOZART, version 2. *Journal of Geophysical Research*, *108*(D24), 4784. https://doi.org/10.1029/2002JD002853

Hozumi, K., Harimaya, T., & Magono, C. (1982). The size distribution of cumulus clouds as a function of cloud amount. *Journal of the Meteorological Society of Japan*, *60*(2), 691–699. https://doi.org/10.2151/jmsj1965.60.2_691

Husain, L. (1989). A technique for determining in-cloud formation of SO_4. *Geophysical Research Letters*, *16*(1), 57–60. https://doi.org/10.1029/GL016i001p00057

Husain, L., Ghauri, B., Yang, K., Khan, A. R., & Rattigan, O. (2004). Application of the SO_4^{2-}/Se tracer technique to study SO_2 oxidation in cloud and fog on a time scale of minutes. *Chemosphere*, *54*(2), 177–183. https://doi.org/10.1016/S0045-6535(03)00531-9

Jacob, D. J. (1986). Chemistry of OH in remote clouds and its role in the production of formic acid and peroxymonosulfate. *Journal of Geophysical Research*, *91*(D9), 9807–9826. https://doi.org/10.1029/JD091iD09p09807

Jacob, D. J., & Wofsy, S. C. (1988). Photochemistry of biogenic emissions over the Amazon forest. *Journal of Geophysical Research*, *93*(D2), 1477–1486. https://doi.org/10.1029/JD093iD02p01477

Karl, T., Guenther, A., Yokelson, R. J., Greenberg, J., Potosnak, M., Blake, D. R., & Artaxo, P. (2007). The tropical forest and fire emissions experiment: Emission, chemistry, and transport of biogenic volatile organic compounds in the lower atmosphere over Amazonia. *Journal of Geophysical Research*, *112*, D18302. https://doi.org/10.1029/2007JD008539

Kim, S. W., Barth, M., & Trainer, M. (2016). Impact of turbulent mixing on isoprene chemistry. *Geophysical Research Letters*, *43*(14), 7701–7708. https://doi.org/10.1002/2016GL069752

Kim, S.-W., M. C. Barth, & C.-H. Moeng (2004). The effect of shallow cumulus convection on the segregation of chemical reactants, paper presented at 16th symposium on boundary layers and turbulence.

Kim, S. W., Barth, M. C., & Trainer, M. (2012). Influence of fair-weather cumulus clouds on isoprene chemistry. *Journal of Geophysical Research*, *117*, D10302. https://doi.org/10.1029/2011JD017099

Krol, M. C., Molemaker, M. J., & de Arellano, J. V. G. (2000). Effects of turbulence and heterogeneous emissions on photochemically active species in the convective boundary layer. *Journal of Geophysical Research*, *105*(D5), 6871–6884. https://doi.org/10.1029/1999JD900958

Laj, P., Fuzzi, S., Facchini, M., Orsi, G., Berner, A., Kruisz, C., … Gallagher, M. (1997). Experimental evidence for in-cloud production of aerosol sulphate. *Atmospheric Environment*, *31*(16), 2503–2514. https://doi.org/10.1016/S1352-2310(96)00217-8

Lelieveld, J., Butler, T. M., Crowley, J. N., Dillon, T. J., Fischer, H., Ganzeveld, L., … Williams, J. (2008). Atmospheric oxidation capacity sustained by a tropical forest. *Nature*, *452*(7188), 737–740. https://doi.org/10.1038/nature06870

Lelieveld, J., & Crutzen, P. (1991). The role of clouds in tropospheric photochemistry. *Journal of Atmospheric Chemistry*, *12*(3), 229–267. https://doi.org/10.1007/BF00048075

Lelieveld, J., & Crutzen, P. J. (1990). Influences of cloud photochemical processes on tropospheric ozone. *Nature*, *343*(6255), 227–233. https://doi.org/10.1038/343227a0

Lenderink, G., Siebesma, A., Cheinet, S., Irons, S., Jones, C. G., Marquet, P., … Sanchez, E. (2004). The diurnal cycle of shallow cumulus clouds over land: A single-column model intercomparison study. *Quarterly Journal of the Royal Meteorological Society*, *130*(604), 3339–3364. https://doi.org/10.1256/qj.03.122

Leriche, M., Pinty, J. P., Mari, C., & Gazen, D. (2013). A cloud chemistry module for the 3-D cloud-resolving mesoscale model Meso-NH with application to idealized cases. *Geoscientific Model Development*, *6*(4), 1275–1298. https://doi.org/10.5194/gmd-6-1275-2013

Li, Y., Barth, M. C., Chen, G., Patton, E. G., Kim, S. W., Wisthaler, A., … Steiner, A. L. (2016). Large-eddy simulation of biogenic VOC chemistry during the DISCOVER-AQ 2011 campaign. *Journal of Geophysical Research: Atmospheres*, *121*(13), 8083–8105. https://doi.org/10.1002/2016JD024942

Liang, J., & Jacob, D. J. (1997). Effect of aqueous phase cloud chemistry on tropospheric ozone. *Journal of Geophysical Research*, *102*(D5), 5993–6001. https://doi.org/10.1029/96JD02957

Lim, Y. B., Tan, Y., Perri, M. J., Seitzinger, S. P., & Turpin, B. J. (2010). Aqueous chemistry and its role in secondary organic aerosol (SOA) formation. *Atmospheric Chemistry and Physics*, *10*(21), 10,521–10,539. https://doi.org/10.5194/acp-10-10521-2010

Madronich, S., & Flocke, S. (1999). The role of solar radiation in atmospheric chemistry. In P. Boule (Ed.), *Environmental photochemistry* (pp. 1–26). Berlin, Heidelberg: Springer. https://doi.org/10.1007/978-3-540-69044-3_1

Marais, E. A., Jacob, D. J., Jimenez, J. L., Campuzano-Jost, P., Day, D. A., Hu, W., & Miller, C. C. (2016). Aqueous-phase mechanism for secondary organic aerosol formation from isoprene: Application to the southeast United States and co-benefit of SO_2 emission controls. *Atmospheric Chemistry and Physics*, *16*(3), 1603–1618. https://doi.org/10.5194/acp-16-1603-2016

McNeill, V. F., Woo, J. L., Kim, D. D., Schwier, A. N., Wannell, N. J., Sumner, A. J., & Barakat, J. M. (2012). Aqueous-phase secondary organic aerosol and Organosulfate formation in atmospheric aerosols: A modeling study. *Environmental Science & Technology*, *46*(15), 8075–8081. https://doi.org/10.1021/es3002986

Millet, D. B., Baasandorj, M., Farmer, D. K., Thornton, J. A., Baumann, K., Brophy, P., … Hu, L. (2015). A large and ubiquitous source of atmospheric formic acid. *Atmospheric Chemistry and Physics*, *15*(11), 6283–6304. https://doi.org/10.5194/acp-15-6283-2015

Moeng, C.-H. (1984). A large-eddy-simulation model for the study of planetary boundary-layer turbulence. *Journal of the Atmospheric Sciences*, *41*(13), 2052–2062. https://doi.org/10.1175/1520-0469(1984)041%3C2052:ALESMF%3E2.0.CO;2

Moeng, C.-H. (1987). Large-eddy simulation of a stratus-topped boundary layer. Part II: Implications for mixed-layer modeling. *Journal of the Atmospheric Sciences*, *44*(12), 1605–1614. https://doi.org/10.1175/1520-0469(1987)044%3C1605:LESOAS%3E2.0.CO;2

Moeng, C.-H., & Sullivan, P. P. (1994). A comparison of shear- and buoyancy-driven planetary boundary layer flows. *Journal of the Atmospheric Sciences*, *51*(7), 999–1022. https://doi.org/10.1175/1520-0469(1994)051%3C0999:ACOSAB%3E2.0.CO;2

Molemaker, M. J., & Vilà-Guerau de Arellano, J. (1998). Control of chemical reactions by convective turbulence in the boundary layer. *Journal of the Atmospheric Sciences*, *55*(4), 568–579. https://doi.org/10.1175/1520-0469(1998)055%3C0568:COCRBC%3E2.0.CO;2

Ouwersloot, H. G., Vilà-Guerau de Arellano, J., van Heerwaarden, C. C., Ganzeveld, L. N., Krol, M. C., & Lelieveld, J. (2011). On the segregation of chemical species in a clear boundary layer over heterogeneous land surfaces. *Atmospheric Chemistry and Physics*, *11*(20), 10,681–10,704. https://doi.org/10.5194/acp-11-10681-2011

Patton, E. G., Sullivan, P. P., & Moeng, C.-H. (2005). The influence of idealized heterogeneity on wet and dry planetary boundary layers coupled to the land surface. *Journal of the Atmospheric Sciences*, *62*(7), 2078–2097. https://doi.org/10.1175/JAS3465.1

Paulot, F., Crounse, J. D., Kjaergaard, H. G., Kürten, A., Clair, J. M. S., Seinfeld, J. H., & Wennberg, P. O. (2009). Unexpected epoxide formation in the gas-phase photooxidation of isoprene. *Science*, *325*(5941), 730–733. https://doi.org/10.1126/science.1172910

Paulot, F., Henze, D., & Wennberg, P. (2012). Impact of the isoprene photochemical cascade on tropical ozone. *Atmospheric Chemistry and Physics*, *12*(3), 1307–1325. https://doi.org/10.5194/acp-12-1307-2012

Paulot, F., Wunch, D., Crounse, J. D., Toon, G. C., Millet, D. B., DeCarlo, P. F., … Wennberg, P. O. (2011). Importance of secondary sources in the atmospheric budgets of formic and acetic acids. *Atmospheric Chemistry and Physics*, *11*(5), 1989–2013. https://doi.org/10.5194/acp-11-1989-2011

Plank, V. G. (1969). The size distribution of cumulus clouds in representative Florida populations. *Journal of Applied Meteorology*, *8*(1), 46–67. https://doi.org/10.1175/1520-0450(1969)008%3C0046:TSDOCC%3E2.0.CO;2

Rienecker, M. M., Suarez, M. J., Gelaro, R., Todling, R., Bacmeister, J., Liu, E., … Woollen, J. (2011). MERRA: NASA's modern-era retrospective analysis for research and applications. *Journal of Climate*, *24*(14), 3624–3648. https://doi.org/10.1175/JCLI-D-11-00015.1

Sander, R. (2015). Compilation of Henry's law constants (version 4.0) for water as solvent. *Atmospheric Chemistry and Physics*, *15*(8), 4399–4981. https://doi.org/10.5194/acp-15-4399-2015

Sander, S. P., Finlayson-Pitts, B. J., Friedl, R. R., Golden, D. M., Huie, R. E., Kolb, C. E., … Ravishankara, R. (2011). Chemical kinetics and photochemical data for use in atmospheric studies: Evaluation number 17 Rep. JPL Publication 10–6. Pasadena, CA: Jet Propulsion Laboratory.

Schumann, U. (1989). Large-eddy simulation of turbulent diffusion with chemical reactions in the convective boundary layer. *Atmospheric Environment (1967)*, *23*(8), 1713–1727. https://doi.org/10.1016/0004-6981(89)90056-5

Sempére, R., & Kawamura, K. (1994). Comparative distributions of dicarboxylic acids and related polar compounds in snow, rain and aerosols from urban atmosphere. *Atmospheric Environment*, *28*(3), 449–459. https://doi.org/10.1016/1352-2310(94)90123-6

Sullivan, P. P., & Patton, E. G. (2011). The effect of mesh resolution on convective boundary layer statistics and structures generated by large-Eddy simulation. *Journal of the Atmospheric Sciences*, *68*(10), 2395–2415. https://doi.org/10.1175/JAS-D-10-05010.1

Sykes, R. I., Parker, S. F., Henn, D. S., & Lewellen, W. S. (1994). Turbulent mixing with chemical reaction in the planetary boundary layer. *Journal of Applied Meteorology*, *33*(7), 825–834. https://doi.org/10.1175/1520-0450(1994)033%3C0825:TMWCRI%3E2.0.CO;2

Tie, X., Madronich, S., Walters, S., Zhang, R., Rasch, P., & Collins, W. (2003). Effect of clouds on photolysis and oxidants in the troposphere. *Journal of Geophysical Research*, *108*(D20), 4642. https://doi.org/10.1029/2003JD003659

Tilgner, A., Bräuer, P., Wolke, R., & Herrmann, H. (2013). Modelling multiphase chemistry in deliquescent erosols and clouds using CAPRAM3.0i. *Journal of Atmospheric Chemistry*, *70*(3), 221–256. https://doi.org/10.1007/s10874-013-9267-4

Tost, H., Lawrence, M. G., Brühl, C., Jöckel, P., The, G. T., & The, S.-O. D. A. T. (2010). Uncertainties in atmospheric chemistry modelling due to convection parameterisations and subsequent scavenging. *Atmospheric Chemistry and Physics*, *10*(4), 1931–1951. https://doi.org/10.5194/acp-10-1931-2010

Tuccella, P., Curci, G., Grell, G., Visconti, G., Crumeroylle, S., Schwarzenboeck, A., & Mensah, A. (2015). A new chemistry option in WRF-Chem v.3.4 for the simulation of direct and indirect aerosol effects using. VBS: Evaluation against IMPACT-EUCAARI data. *Geoscientific Model Development*, *8*(9), 2749–2776. https://doi.org/10.5194/gmd-8-2749-2015

Verver, G. H. L., Van Dop, H., & Holtslag, A. A. M. (1997). Turbulent mixing of reactive gases in the convective boundary layer. *Boundary-Layer Meteorology*, *85*(2), 197–222. https://doi.org/10.1023/A:1000414710372

Vilà-Guerau de Arellano, J., Kim, S. W., Barth, M. C., & Patton, E. G. (2005). Transport and chemical transformations influenced by shallow cumulus over land. *Atmospheric Chemistry and Physics*, *5*(12), 3219–3231. https://doi.org/10.5194/acp-5-3219-2005

Vinuesa, J.-F., & De Arellano, J. V.-G. (2003). Fluxes and (co-)variances of reacting scalars in the convective boundary layer. *Tellus B*, *55*(4), 935–949. https://doi.org/10.1046/j.1435-6935.2003.00073.x

Vinuesa, J. F., & Porté-Agel, F. (2005). A dynamic similarity subgrid model for chemical transformations in large-eddy simulation of the atmospheric boundary layer. *Geophysical Research Letters*, *32*, L03814. https://doi.org/10.1029/2004GL021349

Vinuesa, J.-F., Porté-Agel, F., Basu, S., & Stoll, R. (2006). Subgrid-scale modeling of reacting scalar fluxes in large-eddy simulations of atmospheric boundary layers. *Environmental Fluid Mechanics*, *6*(2), 115–131. https://doi.org/10.1007/s10652-005-6020-9

Wang, K., Zhang, Y., Yahya, K., Wu, S.-Y., & Grell, G. (2015). Implementation and initial application of new chemistry-aerosol options in WRF/Chem for simulating secondary organic aerosols and aerosol indirect effects for regional air quality. *Atmospheric Environment*, *115*, 716–732. https://doi.org/10.1016/j.atmosenv.2014.12.007

Wolfe, G., Hanisco, T., Arkinson, H., Bui, T., Crounse, J., Dean-Day, J., … Huey, G. (2015). Quantifying sources and sinks of reactive gases in the lower atmosphere using airborne flux observations. *Geophysical Research Letters*, *42*(19), 8231–8240. https://doi.org/10.1002/2015GL065839